AGU PUBLICATIONS

JGR

Journal of Geophysical Research: Atmospheres

RESEARCH ARTICLE
10.1002/2013JD021262

Key Points:
- Subcloud top phase determined via shortwave infrared reflectance
- Satellite algorithm for daytime global mixed-phase cloud characterization
- "Cloud phase sounding" enabled from passive radiometer observations

Correspondence to:
S. D. Miller,
Steven.Miller@ColoState.EDU

Citation:
Miller, S. D., Y.-J. Noh, and A. K. Heidinger (2014), Liquid-top mixed-phase cloud detection from shortwave-infrared satellite radiometer observations: A physical basis, *J. Geophys. Res. Atmos.*, *119*, 8245–8267, doi:10.1002/2013JD021262.

Received 26 NOV 2013
Accepted 10 JUN 2014
Accepted article online 13 JUN 2014
Published online 8 JUL 2014

Liquid-top mixed-phase cloud detection from shortwave-infrared satellite radiometer observations: A physical basis

Steven D. Miller[1], Yoo-Jeong Noh[1], and Andrew K. Heidinger[2]

[1]Cooperative Institute for Research in the Atmosphere, Colorado State University, Fort Collins, Colorado, USA, [2]National Oceanic and Atmospheric Administration, National Environmental Satellite, Data and Information Service, Center for Satellite Applications and Research, Advanced Satellite Products Branch, University of Wisconsin-Madison, Madison, Wisconsin, USA

Abstract Meteorological clouds often exist in the liquid phase at temperatures below 0°C. Traditionally, satellite-derived information on cloud phase comes from narrow bands in the shortwave and thermal infrared, with sensitivity biased strongly toward cloud top. In situ observations suggest an abundance of clouds having supercooled liquid water at their tops but a predominantly ice phase residing below. Satellites may report these clouds simply as supercooled liquid, with no further information regarding the presence of a subcloud top ice phase. Here we describe a physical basis for the detection of liquid-top mixed-phase clouds from passive satellite radiometer observations. The algorithm makes use of reflected sunlight in narrow bands at 1.6 and 2.25 μm to optically probe below liquid-topped clouds and determine phase. Detection is predicated on differential absorption properties between liquid and ice particles, accounting for varying Sun/sensor geometry and cloud optical properties. When tested on numerical weather prediction model simulated cloud fields, the algorithm provided threat scores in the 0.6–0.8 range and false alarm rates in the 0.1–0.2 range. A case study based on surface and satellite observations of liquid-top mixed-phase clouds in northern Alaska was also examined. Preliminary results indicate promising potential for distinction between supercooled liquid-top phase clouds with and without an underlying mixed-phase component.

1. Introduction

Between the temperatures of melting (0°C) and homogeneous freezing (about −36°C), meteorological clouds may be composed of liquid droplets, ice crystals, or a mixture of the two [*Rauber and Tokay*, 1991]. The presence of liquid droplets at temperatures below 0°C is, in fact, a commonplace in nature, particularly so at high latitudes [e.g., *Verlinde et al.*, 2007] and for midlevel cloud types [*Wang et al.*, 2004]. However, our understanding of mixed-phase cloud structures, the processes governing their formation, and our ability to properly represent their distribution and important feedback processes (e.g., their atmospheric radiative heating and cooling effects) in numerical weather and climate prediction models are at present very limited [*Sun and Shine*, 1994; *Fowler et al.*, 1996; *Beesley and Moritz*, 1999; *Harrington et al.*, 1999; *Klein et al.*, 2009]. Given the global ubiquity of mixed-phase clouds, satellite remote sensing based methods are best suited to their continuous monitoring and characterization, with the expectation that improved understanding will lead commensurately to improved description of these cloud related processes in forecast models via explicit or parameterized representation.

Knowledge of supercooled liquid water clouds is also critically important to the aviation community, as the droplets from these clouds will freeze on contact with an aircraft frame whose skin temperature is below freezing. This can lead to rapid accumulation of ice with adverse impacts to flight performance due to increased weight and drag, a condition referred to as airframe icing [*Civil Aviation Authority*, 2000]. Icing that develops as a result of accumulating numerous small cloud droplets is termed "rime icing," and the accumulation appears opaque (due to numerous air pockets within the slowly accumulating ice layer). The accumulation of very large supercooled liquid drops (which may be found more often within the stronger updraft cores of convective clouds but may also be present in drizzling stratiform clouds) produce a more hazardous form of "clear icing" (higher water content and fewer air pockets). Small aircraft, including private commuter and unmanned aircraft systems, which seldom are equipped with the necessary boots and heaters

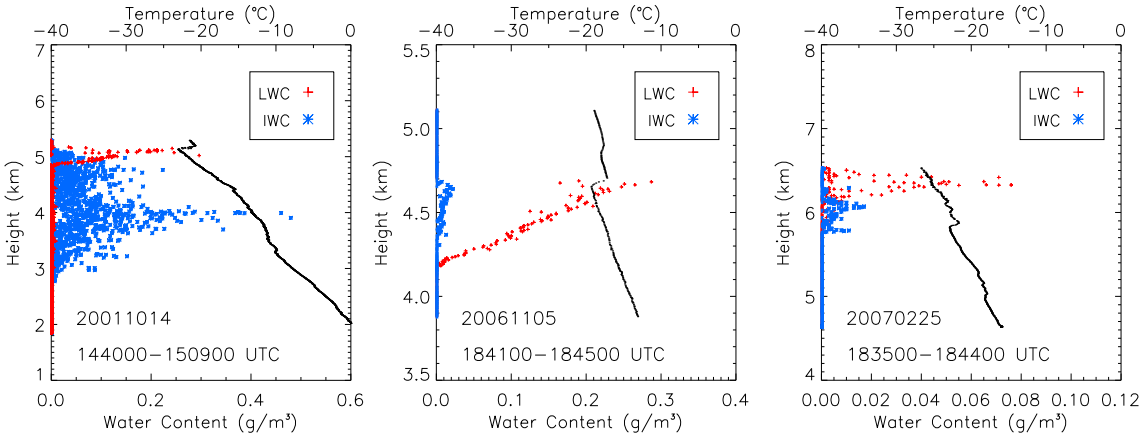

Figure 1. (left to right) Example aircraft in situ measurements of LTMP clouds collected during CLEX-9 and CLEX-10 field campaigns.

for removing this ice in flight, are particularly vulnerable to both forms of icing. Many commercial aircraft are equipped with deicing equipment at the fronts of their wings and contend effectively with rime icing. However, the larger droplets associated with clear icing do not freeze immediately upon contact, streaming instead toward the rear of the aircraft wing prior to freezing completely. This ice accumulates on parts of the wing where standard deicing equipment may not be present or perform as effectively—thus posing an unmitigated hazard.

Research aircraft carrying in situ particle probe sensors have observed that some supercooled/mixed-phase clouds at middle and high latitudes possess a vertical structure where supercooled liquid droplets reside near cloud top while a predominately ice phase (mixed, oftentimes precipitating) exists below cloud top [e.g., *Fleishauer et al*., 2002; *Niu et al*., 2008; *Shupe et al*., 2008]. This liquid-top mixed-phase (hereafter, LTMP) structure is also very common to mixed-phase boundary layer clouds in the Arctic [e.g., *Curry et al*., 1996; *Pinto*, 1998; *Wang et al*., 2004; *Shupe et al*., 2006; *Liu et al*., 2007; *Verlinde et al*., 2007]. Example in situ measurements of such LTMP clouds at midlatitudes, collected via aircraft during the 9th and 10th Cloud Layer Experiments (CLEX) [*Carey et al*., 2008; *Ou et al*., 2009; *Noh et al*., 2011, 2013], are shown in Figure 1. Earlier cases examined by *Fleishauer et al*. [2002] during the 5th CLEX were geometrically thin (on the order of 0.5 km thick) clouds with only modest liquid water contents (0.01–0.15 g m^{-3}), with single-layered clouds showing the greatest tendency for exhibiting the LTMP structure. The dominance of the ice phase observed in the multilayered cloud systems was postulated to be due to seeder-feeder mechanisms (i.e., ice precipitating from upper "seeder" cloud layers serving as sources of ice condensation nuclei to the lower layers) [e.g., *Schneider and Moneypenny*, 2002]. In that case, the lower "feeder" cloud layers would usually be obscured to passive satellite-observing systems due to the overriding seeder cloud layers, precluding detection.

The physical mechanisms responsible for producing LTMP clouds, and the frequency/scale/distribution of occurrence of all such clouds globally, are not well understood. The structure may, in fact, be a transient one, related to the critical point where an initially all supercooled liquid cloud glaciates via vapor deposition on ice growing at the expense of water drops (the Wegener-Bergeron-Findeisen process) [e.g., *Bergeron*, 1935] and secondary ice particle formation via rime splintering [e.g., *Mossop et al*., 1970; *Hallett and Mossop*, 1974]. *Hu et al*. [2010] show large amounts of supercooled liquid water clouds at high latitudes, especially over the relatively pristine maritime air mass of the Southern Ocean. *Trenberth and Fasullo* [2010] suggest that there exist biases in top-of-atmosphere net radiative forcing for Coupled Model Intercomparison Project Phase 3 [*Meehl et al*., 2007] simulations in the Southern Ocean, tied to problems with cloud representation. Given that the Southern Ocean has the highest observed cloud fraction in the world [*Mace et al*., 2007], uncertainties in the nature of mixed-phase clouds in this expansive and poorly observed region further motivate the need for improved satellite-based cloud phase characterization tools.

Still, many questions surround the LTMP cloud structure: Under what meteorological and aerosol conditions do such clouds form? Is there a regional, seasonal, or diurnal dependency? Does this structure indeed represent a short-lived, transient state, or are they longer-lived and hence radiatively far more significant?

What fraction of supercooled liquid-top clouds, as identified by current passive satellite sensor methods, is, in fact, LTMP? Do the properties of these clouds introduce any particular hazards to aircraft in terms of icing threat (e.g., larger droplet size), or does their lower liquid water path through the cloudy column offer a relatively safe pathway for transit amidst a surrounding field of purely supercooled clouds? While these questions serve as basic motivation for the current research, our objective is to not to answer them here. Instead, we seek to provide an improved observational basis for doing so. Whereas in situ measurements can address many of the process-related questions posed above, such observations are costly, spatially limited, and highly impractical. If a tractable strategy for detection via passive radiometry were identified, satellite remote sensing would provide an ideal platform for observing the distribution of LTMP clouds globally.

Here we present a daytime multispectral algorithm that attempts to identify and characterize LTMP clouds. The algorithm is applied to the subset of clouds in the scene that are determined a priori, based on conventional passive radiometer phase-determination techniques, to be supercooled liquid top. The algorithm was designed to be applicable to optical-spectrum satellite imaging radiometers and in particular to the future high-temporal/spectral resolution Geostationary Operational Environmental Satellite (GOES)-R series Advanced Baseline Imager (ABI) [*Schmit et al.*, 2005]. It exploits differential absorption properties between liquid and ice particles in different atmospheric window bands in the shortwave-infrared (SIR; 1–3 μm where thermal emission signals from meteorological parameters are considered small) part of the electromagnetic spectrum using reflectance measurements whose weighting functions peak below the cloud top. Comparing these measurements to those that would be expected for an entirely liquid phase cloud (based on radiative transfer simulations), conservative thresholds are used to identify cases where a subcloud top ice/mixed-phase layer is likely to be present.

The paper is structured as follows: Section 2 provides a background of passive remote sensing methods geared toward cloud properties and internal structure, section 3 details the physical basis for the current approach, section 4 develops a detection and characterization algorithm based on these physics, section 5 assesses the instantaneous and statistical performance when applying the algorithm to simulated observations from a numerical weather prediction model, section 6 presents initial results from an observational case study, and section 7 concludes the paper with general considerations of the algorithm's strengths, limitations and potential utility for application on satellite observing systems on the near horizon.

2. Cloud Phase Determination and Passive Profiling

The scientific literature is replete with examples showing the utility and versatility of satellite-based radiometers for detecting and characterizing the macrophysical, microphysical, and optical properties of global cloudiness. Multispectral narrowband measurements spanning the optical spectrum (i.e., 0.4 to 14 μm) are used to determine cloud occurrence, classify cloud type, and retrieve cloud top height/pressure, integrated liquid/ice water content, cloud emissivity, and cloud top microphysics [e.g., *Nakajima and King*, 1990; *Inoue and Ackerman*, 2002; *Platnick et al.*, 2003]. Airframe icing conditions, as mentioned previously, are directly related to these properties [*Cober et al.*, 1995; *Mecikalski et al.*, 2007].

Passive satellite radiometer observations also provide information about cloud top phase. Detection of supercooled liquid water clouds during the daytime [e.g., *Ellrod*, 1996; *Lee et al.*, 1997; *Ellrod and Bailey*, 2007] is predicated on differential scattering/absorption properties between the liquid and ice in the midwave infrared window (MIR, e.g., 3.9 μm), coupled with a measurement of thermal infrared window (TIR, e.g., 11.0 μm). The MIR reflectance of sunlight is greater for liquid cloud droplets, owing to a higher complex index of refraction (proportional to absorption) for ice at this wavelength. Thresholds placed on the MIR reflectance, determined conservatively from radiative transfer simulations of liquid- and ice-topped clouds, are used to determine cloud top phase. Under the assumption of an optically thick cloud emitting as a blackbody in the TIR band (reasonable for most liquid phase clouds), the TIR brightness temperature is a good approximation of the cloud top temperature. If this temperature is less than 0°C and the cloud top phase was evaluated as liquid, based on the MIR reflectance thresholds, then a supercooled liquid water classification is inferred. The classification is often referred to as "mixed phase" (liquid + ice) due to uncertainties in the thresholds assumed.

Cloud phase information is also available via a combination of the 8.5, 11, and 12 μm bands [*Strabala et al.*, 1994; *Baum et al.*, 2000; *Pavolonis*, 2010]. The benefit of infrared-only techniques is the ability to apply the

algorithms to both daytime and nighttime observations. Owing to strong absorption of liquid and ice water at these thermal infrared wavelengths [e.g., *Hu and Stamnes*, 1993], the phase information typically corresponds to conditions near cloud top (i.e., visible optical thickness of ~1.0 into the cloud, or typically the first few hundred meters) [*Pavolonis et al*., 2005]. Thus, both the MIR and TIR band techniques would potentially classify some LTMP clouds simply as "supercooled liquid." The objective of the current algorithm is to enlist additional bands in the SIR part of the spectrum that are capable of probing below cloud top, to deeper levels within the cloud, in an effort to identify the subset of these liquid-topped clouds that exhibit signs of LTMP structure.

This algorithm is predicated on the well-established principles of atmospheric temperature and moisture profiling (sounding) by passive satellite radiometers [e.g., *Smith et al*., 1972; *Susskind et al*., 2003]. Conventional sounding techniques utilize measurements in spectral bands where the atmosphere absorbs/emits, as opposed to the "clean window" bands where the atmosphere is more transparent. Curves of differential transmittance with height, called weighting functions, describe the balance between gaseous species abundance (increasing toward the surface) and the optical path to space (increasing toward the top of the atmosphere) at the spectral band in question. For a well-mixed atmospheric gas like carbon dioxide, the weighting functions typically are bell shaped in the vertical, with the peak of the function denoting the principal atmospheric level contributing to the measurement. Weighting functions for spectral bands where the atmosphere is less opaque will peak closer to the surface (or may intersect with it, denoting a strong surface contribution to the measurement), while those corresponding to more opaque bands peak higher up in the atmosphere. Conventionally, satellite-based soundings are applied to clear-sky scenes. When hyperspectral measurements are available, providing the ability to craft optimal weighting functions, above-cloud soundings [e.g., *Weisz et al*., 2007] can be attempted.

Other studies have applied the principles of sounding to measurements in optically thick scattering/absorbing media, such as meteorological clouds. In-cloud weighting function structures, analogous to those characteristic of the tenuous atmosphere but compacted in geometric extent, exist for SIR bands where clouds possess both scattering and absorption characteristics. The sensitivity becomes broader in the vertical, probing to deeper levels within the optically thick cloud media, at shorter (and less absorbing) wavelengths. *Nakajima and King* [1990] define a procedure for adjusting cloud effective radius retrievals from the Advanced Very High Resolution Radiometer to arbitrary levels within the cloud in order to provide more representative comparisons against in situ (i.e., at flight levels somewhere below cloud top) observations. *Miller et al*. [2001] apply this same procedure to compare cloud particle size retrievals from GOES to instrumented aircraft observations in drizzling marine stratocumulus and in a similar way adjust 94 GHz radar-derived cloud particle sizes to reconcile them with GOES retrievals in tropical cirrus. *Platnick* [2000] examines the effects of vertical photon transport in the context of cloud microphysical retrievals for various droplet size profiles, showing strong sensitivity to SIR observation band due to the differential probing depths of the weighting functions. *King and Vaughan* [2012] expand on this concept in showing how hyperspectral measurements can further improve upon such SIR-based profiling methods. *Chang and Li* [2002, 2003] examine and retrieve vertical profiles of cloud droplet effective radius using a combination of SIR and MIR bands, *Nakajima et al*. [2010a, 2010b] use Moderate Resolution Imaging Spectroradiometer (MODIS) [*Platnick et al*., 2003] and CloudSat [*Stephens et al*., 2002] data to study profiles of droplet growth in warm water clouds, and *Nagao et al*. [2013] use multispectral SIR and MIR observations to examine the vertical structures of liquid water clouds. *Zhang* [2013] applies a bispectral method involving 1.6 and 2.1 μm band reflectance from MODIS to identify the presence of a warm-rain process influenced droplet size distribution near the bases of clouds. In these previous studies, the phase cloud is assumed to be vertically and horizontally homogeneous.

3. Physical Basis

When clouds transition to a mixed-phase state (either due to homogeneous freezing of supercooled liquid water droplets or due to introduction/activation of suitable ice condensation nuclei), ice crystals begin to grow rapidly at the expense of liquid drops [*Wegener*, 1911; *Bergeron*, 1935; *Findeisen*, 1938]. This preferential ice crystal growth is due to a lower equilibrium vapor pressure over ice surfaces, such that in the absence of vertical motion the cloud particles would evolve rapidly toward a predominantly ice phase. In the case a mixed-phase cloud forming under conditions weak/steady vertical ascent, it is possible for the mixed phase to decouple via sedimentation; the growing ice crystal population will descend to lower portions of the cloud (producing ice virga), such that over time the cloud evolves into the LTMP structure.

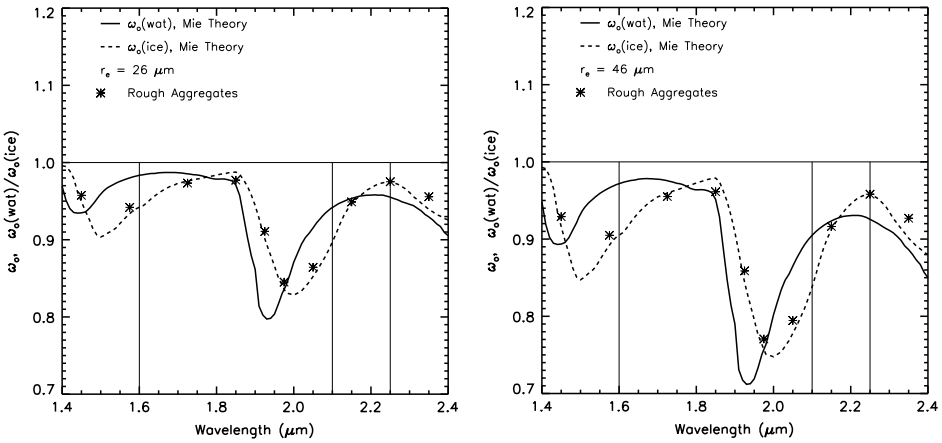

Figure 2. Single-scattering albedo (ω_o) across SIR wavelengths for liquid and ice phases with effective radii = (left) 26 μm and (right) 46 μm. Atmospheric window bands centering on 1.6, 2.1, and 2.25 μm are shown. Note the reversal in scattering behaviors for water and between 1.6 and 2.25 μm.

The ability to detect LTMP clouds during the daytime from passive satellite radiometers is predicated on the differential scattering/absorption properties of the liquid and ice at specific bands. Figure 2 presents a spectrum of single-scattering albedo (ω_o) for liquid and ice phases (based on Mie theory; spherical particles), showing marked differences between the spectral behaviors of ice and liquid in the SIR part of the spectrum. In particular, we note that ice is more absorbing than liquid at $\lambda = 1.6$ μm while liquid is more absorbing than ice at $\lambda = 2.25$ μm. Effective radii of 26 μm and 46 μm illustrate how the differential scattering/absorption behavior is preserved and, in fact, becomes even more pronounced with increasing particle size. The behavior with respect to nonspherical ice habits is discussed in more detail in section 4.

Figure 3 shows an example of in-cloud weighting functions (a metric of sensitivity, denoting where in the vertical the principal measurement information is coming from) calculated for selected SIR bands and the 3.9 μm MIR band for different cloud particle sizes with Sun directly overhead and a nadir-viewing angle. The degree of vertical photon transport, which defines the structure of the weighting functions, depends on the vertically distributed cloud properties, measurement wavelength, and the Sun/sensor geometry [cf *Platnick*,

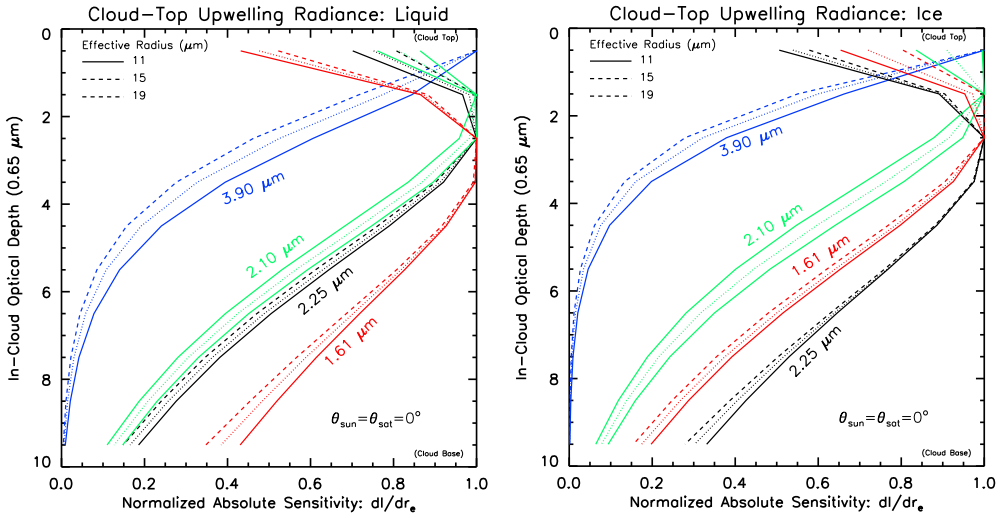

Figure 3. Sensitivity of cloud top upwelling radiance to in-cloud perturbations at various levels (weighting function) for selected SIR and MIR atmospheric window bands in (left) liquid and (right) ice clouds. For both clouds, the 1.6 and 2.25 μm sensitivities peak at optical thickness of ~2–3 below cloud top. The reversal in water versus ice cloud probing for these two bands is consistent with the single scatter albedo properties shown in Figure 2.

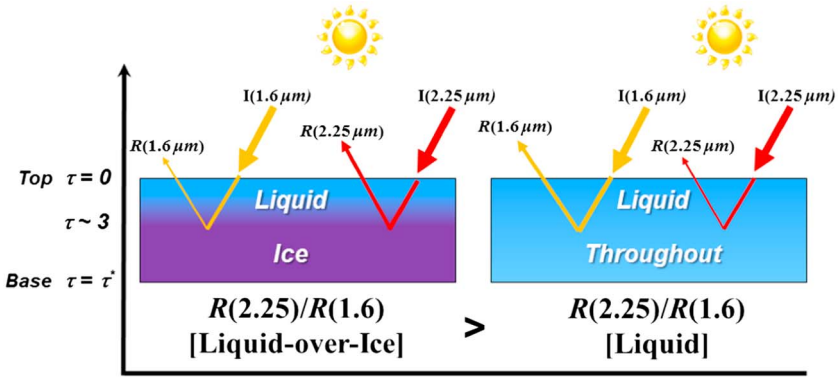

Figure 4. The effect of differential radiative properties for liquid and ice phases at SIR bands (as in Figure 2) when considering reflectance ratios for (left) LTMP clouds and (right) pure liquid phase clouds. The thickness of the upwelling arrows represents (notionally) the relative intensity of reflected light at each wavelength for a given cloud phase structure. The optical thickness of $\tau \sim 3$ corresponds to peak of weighting functions as shown in Figure 3, but sensitivity to phase information at deeper levels below cloud top exists for both bands, resulting in a gradual tapering off of reflectance ratio sensitivity with increasing liquid-top optical thickness.

2000, Figure 5a]. The weighting functions in Figure 3 were produced by perturbing the extinction coefficient at discrete levels within an idealized plane-parallel (horizontally uniform) cloud using a doubling/adding radiative transfer model [*Miller et al.*, 2000]. The 1.6, 2.1, and 2.25 μm SIR bands are seen to have considerably higher sensitivity to the inner portions of the cloud (higher scattering and thus deeper penetration below cloud top) in contrast to the MIR band reflectance, which is seen to be most sensitive to near cloud top. This cloud top sensitivity in the 3.9 μm weighting function peak is due to strong absorption of liquid water droplets. Even stronger absorption by liquid water in the thermal infrared bands (e.g., the "trispectral" 8.5, 10.35, and 12.3 μm TIR bands, which also are used for cloud top phase determination) [*Strabala et al.*, 1994; *Pavolonis*, 2010] biases the assertion of cloud phase to the upper most portions of the cloud (~1.0 visible wavelength optical thickness [*Pavolonis et al.*, 2005]). Hence, the shortwave SIR bands provide unique insight on cloud internal structure which the current algorithm attempts to exploit.

Figure 4 illustrates conceptually the physical basis for the algorithm. We examine the solar reflectance at two wavelengths whose weighting functions peak below cloud top (probing the cloud in a way that is analogous to how temperature/moisture sounding algorithms probe the clear-sky atmosphere). For the current algorithm, we have selected the 1.6 and 2.25 μm atmospheric window bands, which probe deeper into the cloud than the 3.9 μm band (Figure 3) and also provide a differential phase signal as shown in Figure 2. To facilitate the assignment of a detection threshold in light of the variability of pure liquid phase clouds, we compare the ratio of these measurements to the expected reflectance behavior of a "pure liquid" cloud having the same total optical thickness and cloud top particle size as was retrieved for the observed cloud. If the difference between the observations and the pure liquid case exceeds certain threshold margins (chosen conservatively, such that the most probable scenario is a strongly absorbing ice phase somewhere below the liquid cloud top), then we infer the presence of an LTMP cloud. Mathematical formulation and details regarding the selection of appropriate thresholds are provided in section 4.

The required 1.6 and 2.25 μm band combination is available on the Visible/Infrared Imaging Radiometer Suite (VIIRS) on *Suomi* National Polar-orbiting Partnership and the future Joint Polar Satellite System satellites, as well as the future Himawari-8 Advanced Himawari Imager (AHI) and GOES-R ABI. Unfortunately, the 2.25 μm band is not present on MODIS, precluding the convenient pairing of MODIS, CloudSat, and CALIPSO for global evaluation of the algorithm on a regular basis. Although their orbital altitudes are different, *Suomi* (824 km) and Aqua (705 km) share a common orbital plane, such that Aqua laps *Suomi* and offers nearly simultaneous observations for several consecutive orbits every ~3 days. It should be noted that a lidar/radar method (e.g., one using CALIPSO and CloudSat, following *Zhang et al.* [2010]) should in principle outperform this passive radiometer technique and is applicable day and night. However, the active sensor method is applicable only to a very limited domain along the curtain observation, in contrast to the full-swath information of a passive technique.

4. Algorithm Description

4.1. Defining the Detection Test

To simulate SIR reflectance measurements for idealized LTMP clouds, radiative transfer calculations for idealized clouds were conducted using the Santa Barbara DISORT Atmospheric Radiative Transfer (SBDART) [*Ricchiazzi et al.*, 1998] model. The radiative transfer model assumes plane-parallel cloud structure and spherical particles (Mie theory). Consideration for the effects of nonspherical ice is discussed in the sensitivity analyses to follow. In the calculations, ocean/vegetation surfaces and rural/ocean aerosol models with midlatitude winter and summer atmospheres were considered. As an approximation to the structures observed in Figure 1, we assumed an idealized cloud vertical structure: a simple two-layer stratified cloud with liquid upper layer and either liquid or ice phase in the lower layer (Figure 4). The upper (liquid) layer was placed between 5 and 5.5 km, and the lower layer was placed between 3 km and 5 km over the surface, based on CLEX-5, CLEX-9, and CLEX-10 in situ aircraft measurements [*Fleishauer et al.*, 2002; *Carey et al.*, 2008; *Noh et al.*, 2011]. The effects of atmospheric transmission were negligible in the current formulation which utilizes atmospheric window bands, but the height of the idealized clouds was selected to match the heights of midlevel mixed-phase clouds observed most often during the CLEX field campaigns.

Properties of the idealized clouds were varied systematically to construct look-up tables (LUTs) of simulated measurements. The total cloud optical thickness ($\tau_{\_total}$) was varied from 0 to 30, and the optical thickness of the top liquid layer ($\tau_{\_liquid}$) component was varied from 0 to 30 with an increment of 1. To examine sensitivity to the top (liquid) layer, cloud drop effective radius of the top layer was specified as 6, 8, 10, 12, 15, and 20 μm with the lower (ice) layer held constant at 30 μm. Likewise, to examine sensitivity of the lower (ice) layer, the effective particle radius of the ice layer was varied from 30, 50, 70, 100, and 120 μm with the radius of the liquid (top) layer held constant as 8 μm. To further expand the solution space, we included several cases having the same effective radii for both top liquid and bottom ice layers, set at 10, 20, 30, and 40 μm. For each input condition, the monochromatic radiances (I_λ) were computed at 10° resolution in sensor zenith angle (0°–80°), Sun/sensor relative azimuth angle (0°–170°), and solar zenith angle (0°–80°). These values were converted to spectral reflectance (R_λ) for use in the algorithm via

$$R_\lambda = \pi I_\lambda / \mu_o F_{o\lambda}, \tag{1}$$

where μ_o is the cosine of the solar zenith angle and $F_{o\lambda}$ is the solar spectral irradiance.

The simulated reflectance ratio LUT was built using the SBDART model for each input over a range of Sun/satellite geometries, total optical thickness, cloud top effective radii, and surface conditions as described above. The final LUT contains over 43 million entries. The reflectance ratio between simulated 2.25 μm and 1.6 μm reflectance values is defined as

$$RR\_SIM = R\_sim(2.25\,\mu\text{m}) \Big/ R\_sim(1.6\,\mu\text{m}). \tag{2}$$

For *RR_SIM*, the total optical thickness is partitioned between the upper (liquid) and lower (ice/mixed) layers for a range of values ($\tau = 0$ to 30), with the extreme cases being all liquid (lower layer $\tau = 0$) and all ice/mixed (top layer $\tau = 0$). By the differential absorption arguments described above and illustrated in Figures 2 and 3, we would expect the reflectance ratio $R(2.25)/R(1.6)$ to have a smaller denominator value when an ice/mixed lower layer is encountered, in contrast to a pure liquid phase cloud. Therefore, we would expect the same behavior to occur in our simulated reflectance ratios when considering a LTMP cloud (*RR_SIM_Mixed*) in comparison to a pure liquid cloud (*RR_SIM_Liquid*). The *RR_SIM_Liquid* values are interpolated from portions of the LUT where the total optical thickness is equal to the liquid optical thickness ($\tau_{\_total} = \tau_{\_liquid}$).

The comparisons between the pure liquid and LTMP cloud simulations are done via the following liquid-normalized reflectance ratio:

$$RR\_SIM\_COMP = RR\_SIM\_LTMP \Big/ RR\_SIM\_Liquid. \tag{3}$$

Figure 5 shows example contour plots of *RR_SIM_COMP* for an example set of viewing geometries (varying sensor zenith angle) as simulated by the radiative transfer model. *RR_SIM_COMP* exhibits higher sensitivity for larger total cloud optical thickness and a relatively optically thin liquid (top) layers. By definition, values of $RR\_SIM\_COMP > 1$ correspond to LTMP clouds. In the limiting case that the liquid layer optical thickness equals the total cloud optical thickness, $RR\_SIM\_COMP = 1.0$. According to these simulations, an LTMP cloud

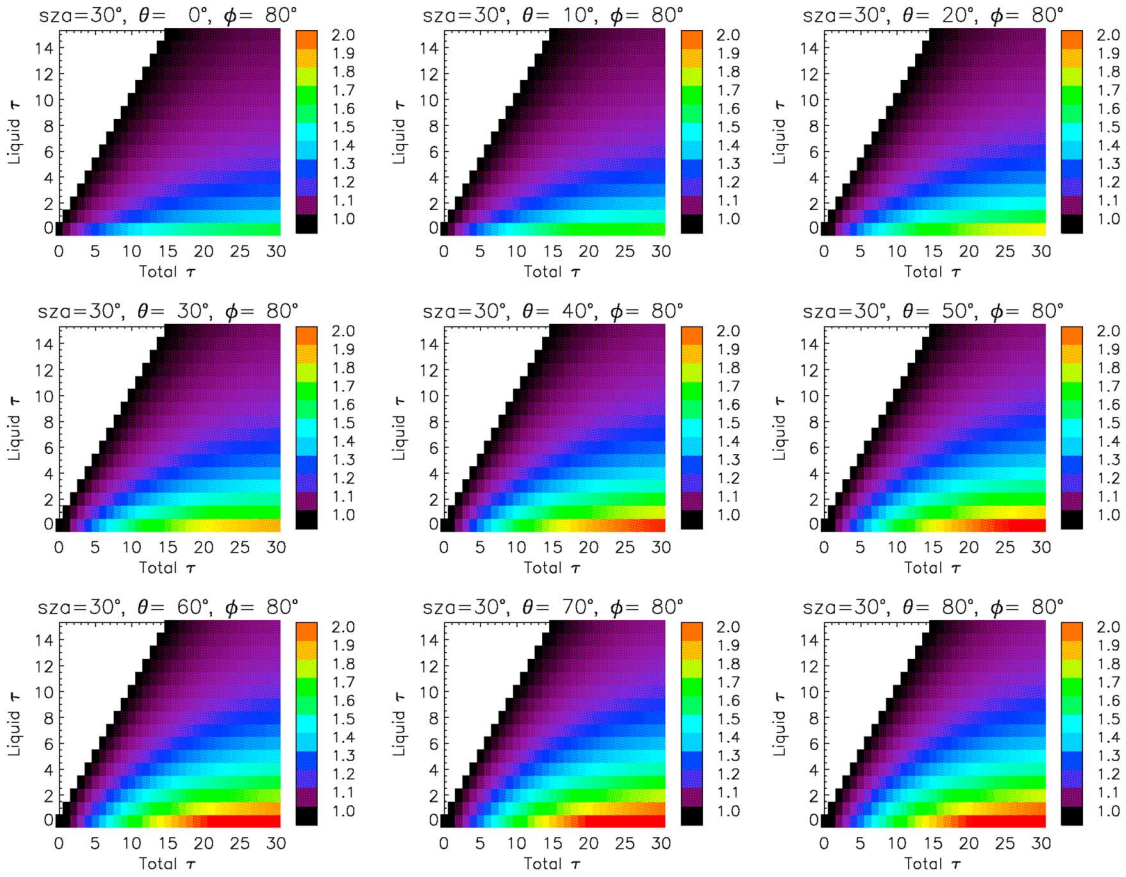

Figure 5. Example family of normalized reflectance ratios (*RR_SIM_COMP*; equation (3)) for an idealized LTMP cloud, as simulated by SBDART for 30° solar zenith angle, 80° relative azimuth angle, and a variety of sensor zenith angles. Cloud particle effective radius for upper (pure liquid phase) and lower (pure ice phase) layers are 10 μm and 30 μm, respectively. Here a pure liquid phase cloud produces a reflectance ratio of unity, while larger values of reflectance ratio arise from the differential absorption properties of subcloud top ice.

will produce a very different (2.25 μm / 1.6 μm) reflectance ratio than an all-liquid cloud. The depth of enhanced cloud top penetration by these two SIR bands depends on the optical thickness of the liquid layer near cloud top and the Sun/sensor geometry.

It is also observed in Figure 5 that values of *RR_SIM_COMP* decrease with increasing cloud top (liquid) layer optical thickness. The physical basis for this decrease in the detection signal is straightforward; the weighting functions used for phase detection (e.g., Figure 3) only penetrate so far below cloud top, such that cloud dominated by liquid phase at cloud top will produce a weaker LTMP signal. On the other hand, the detection signal is seen to increase with optically thinner cloud top liquid phase. This signal is maximized in the extreme case when the liquid-top component of the total optical depth approaches zero (i.e., the estimated signal that would be produced by a comparison between pure liquid and pure ice clouds). However, the current algorithm will never evaluate such clouds, since a precondition of the detection is that the cloud has been determined to have liquid-top phase (implying the presence of a liquid phase optical thickness of at least 1.0) [*Pavolonis et al.*, 2005].

For analysis of satellite SIR reflectance observations (*R_sat*), we define a liquid normalized reflectance ratio, *RR_OBS_COMP*, as

$$RR\_OBS\_COMP = RR\_OBS \Big/ RR\_SIM\_Liquid, \tag{4}$$

where, similar to equation (2),

$$RR\_OBS = R\_sat(2.25\,\mu m) \Big/ R\_sat(1.6\,\mu m) \tag{5}$$

and *RR_SIM_Liquid* is taken from the LUTs for the case of ($\tau_{\_total} = \tau_{\_liquid}$), using the retrieved $\tau_{\_total}$ and cloud top effective particle size to interrogate the LUT. Normalization by *RR_SIM_Liquid* provides a reference point for the observations. When *RR_OBS_COMP* is found to exceed a specified threshold, *RR_THRESH* (discussed below), the algorithm returns a positive detection for a LTMP cloud at that location.

4.2. Consideration of Realistic Ice Crystal Habits

Whereas the spherical particle assumption is reasonable for the cloud top liquid layer, it fails to capture the complex single scatter behaviors of real ice morphologies. Since the ice layer is assumed to reside below a semioptically thick ($\tau > \sim 1.0$) scattering liquid-top layer, the details of the ice-scattering phase function are suppressed, and the global reflectance and transmittance are governed more by the single scatter albedo and asymmetry parameter of the bulk cloud properties. It is worth demonstrating, however, that the bulk scattering properties for more representative complex ice morphologies are preserved in a spherical particle assumption, thereby maintaining a physical basis for phase discrimination.

Yang et al. [2000] supply a full representation of the scattering properties for a variety of ice crystal morphologies over a wide range of effective particle size and wavelengths across the visible to thermal infrared. *Baran et al*. [2005] demonstrate that idealized geometries of pristine ice crystal habits do not represent multiangle satellite observations of real clouds as well as does an ensemble of randomly oriented habits. As such, we used the rough aggregate species from *Yang et al*. [2000] for our simulations.

Figure 2 includes values of spectral single scatter albedo for these rough aggregates (plotted as asterisks at selected wavelengths). While some differences exist in comparison to Mie theory for ice spheres (dashed line), the comparisons exhibit an overall similar behavior in terms of both spectral and particle size variations. The general consistency and increasing strength of the signal with increasing particle size suggests that vertical variation of the lower ice layer(s) will indeed modulate, but not introduce reverse the sign of, the reflectance-ratio signal exploited by the current algorithm. This finding might be expected since the bulk properties depend principally on the particle phase as opposed to the details of directional scattering.

The underpinning hypothesis of the current algorithm is that the differential bulk scattering properties are what should determine the presence of an ice-phase signal beneath the $\tau > 1$ cloud top liquid layer. Specifically, the ratio $\omega_o(2.25)/\omega_o(1.6)$ should be less than unity for liquid phase and greater than unity for ice phase. A robust signal should produce this same relationship for a variety of ice crystal habits and sizes (considering vertical inhomogeneity). Figure 6 shows single scatter albedo ratio variation for liquid droplets and ice spheres (Mie) and the full complement of *Yang et al*. [2000] ice crystal habits. With the exception of dendritic habits, which show a slight departure to subunity values for small crystals, the majority of ratios exhibit a similar behavior to the spherical ice approximation (and particularly so for the aggregate species). Meanwhile, the ratios for the liquid droplets are suppressed for larger droplet sizes.

We also assessed the ability of the aggregate ice crystal phase function to reproduce the normalized 2.25/1.6 μm reflectance ratios used for detection of LTMP clouds in the current algorithm. Doing so required extraction of the *Yang et al*. [2000] phase functions for the two spectral bands and representing them numerically in the RTM. We selected an effective particle size of 36 μm for this exercise. The strong forward peaked nature of these phase functions required usage of the delta-M scaling method [*Wiscombe*, 1977], wherein the forward scattering lobe is approximated as a δ-function. A Legendre polynomial expansion was fit to the scaled phase function, and the resultant expansion coefficients were incorporated into the RTM. Correct implementation of this method in the RTM used for this exercise has been demonstrated previously by *Miller et al*. [2000]. The general structure of reflectance ratios simulated via the above process (not shown) is consistent with the Mie-based simulations, confirming that the bulk scattering and absorption properties of the ice phase (ω_o) dominate the signal as opposed to the details of directional scattering.

4.3. Subpixel Heterogeneity

Subpixel cloud heterogeneity is a recognized challenge to most satellite-based cloud detection, type/phase classification, and optical property retrieval algorithms. In the current algorithm, heterogeneity may become particularly important over certain land surfaces where stronger emissivity differences may exist between 1.61 μm and 2.25 μm. Over ocean, the reflectance is low, but the dark water background could present a greater challenge for a single-band technique—where the absolute value of reflectance would be suppressed in the presence of heterogeneity. Part of the reason for implementing a reflectance *ratio*, as

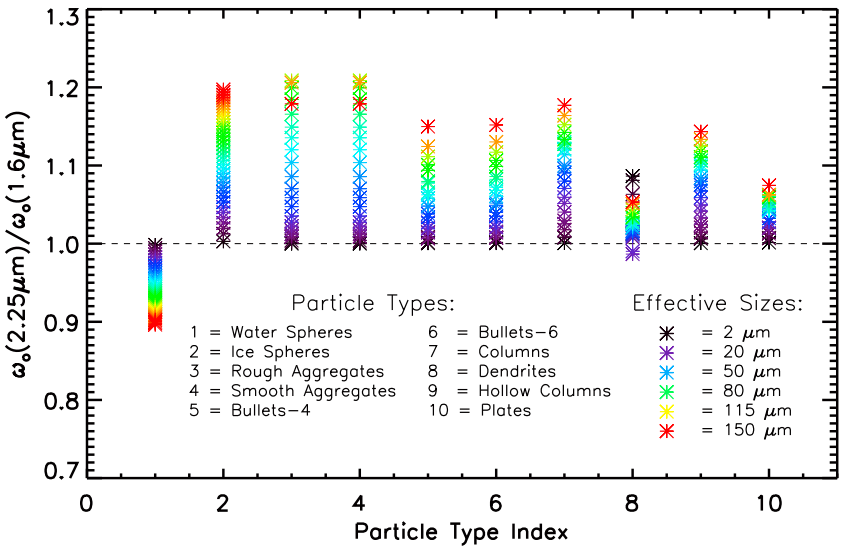

Figure 6. Spectral single scatter albedo ratios for a family of ice crystal sizes and habits. Water and ice spheres are from Mie theory. Most ice crystal habits and effective sizes exhibit inverse behavior to the liquid phase, with strength increasing with particle size. Ice spheres bear closest resemblance to aggregates and columns.

opposed to simply comparing either the 1.61 μm or 2.25 μm against a simulated pure liquid cloud signal, was to mitigate such heterogeneity effects.

4.3. Sensitivity to Drizzle

"Liquid over drizzle" cloud scenarios (e.g., drizzling marine stratocumulus) were also considered in order to determine whether enhanced absorption due to the presence of drizzle at lower levels of the cloud might be misconstrued for the presence of ice when applying our algorithm thresholds. The radiative transfer model calculations were performed with the same solar/sensor geometry information as before, but with the top liquid layer with effective radius set to 12 μm and bottom layers being all-liquid with each effective radii ranging from 12 to 120 μm (following *Kogan and Kogan* [2001]). As anticipated from the bulk scattering properties for water droplets at 1.61 μm and 2.25 μm (larger drizzle droplets have a lower single scatter albedo at 2.25 μm than the smaller cloud droplets, continuing the trend seen in Figure 2), the simulations confirm that the presence of drizzle, in fact, further reduces the observable 2.25 μm/1.61 μm reflectance ratio below values of unity. It was found that over 98% liquid over drizzle cases were excluded when *RR_THRESH* was set to a value greater than 1.1, or less than 2% misclassified as LTMP in the detection algorithm due to the presence of drizzle.

4.4. Threshold Determination

We must specify our detection threshold (*RR_THRESH*) conservatively (i.e., to avoid false alarms in LTMP detection, but not so conservative as to result in significant missed detections) in order to account for uncertainties such as the vertical distribution of cloud particle size (which could alter the strength of absorption). As a simple first-order solution, the selection of a conservative threshold can be approached via statistical analysis of the LUT information. Here we determined *RR_THRESH* by constructing cumulative distribution functions (CDFs) of the liquid-normalized reflectance ratios (*RR_SIM_COMP*) for all LTMP clouds in the LUT. The results, shown in Figure 7, indicate that 80% of all LTMP clouds were accounted for when *RR_THRESH* = 1.27, and 92% when *RR_THRESH* = 1.50. For LTMP clouds having optical thickness greater than 10 but the top (assumed liquid) layer optical thickness less than 5 (referred to in Figure 7 as "shallow liquid top"), 70% of all cases are detected with *RR_THRESH* = 1.50, and 80% when *RR_THRESH* = 1.625.

It can be seen in Figure 5 that a given *RR_THRESH* threshold may never be exceeded unless a minimum total cloud optical thickness, *OT**, is present. In other words, *OT** corresponds to the critical point where our selected threshold *RR_THRESH* value intersects the horizontal axes in Figure 5. Based on our radiative transfer simulations, any cloud pixels having total optical thickness less than *OT** would never produce observed

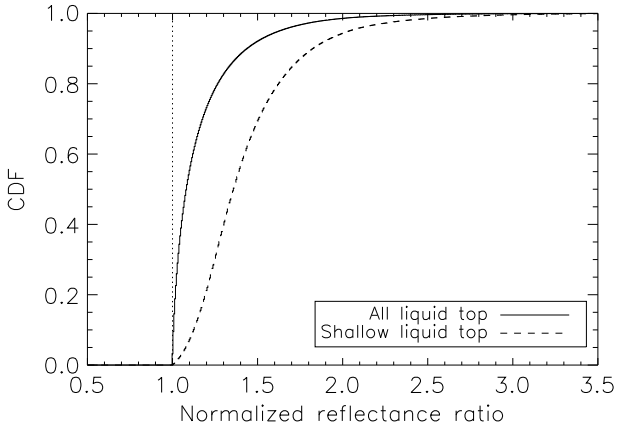

Figure 7. Cumulative distribution functions of simulated liquid-normalized reflectance ratios (*RR_SIM_COMP*; equation (3)) for LTMP clouds. Solid curve: all clouds in the LUT database, dashed curve: the subset of clouds having total cloud optical thickness greater than 10 and a liquid-top optical thickness component ranging between 1 and 5.

RR_OBS_COMP values that are large enough to exceed *RR_THRESH* and hence be able to trigger a "detection" in our algorithm (even if the cloud structure was indeed LTMP). Following *Pavolonis et al.* [2005], we assumed that any cloud that is classified by conventional MIR and TIR band techniques as being supercooled liquid top will have a visible optical thickness of at least 1.0 and thus required $OT^* \geq 1$. The exact value of *OT** changes as a function of the cloud top effective radius (via the asymmetry parameter which determines the degree of forward scatter within the medium) and the level of confidence we impose on the detection (determined by *RR_THRESH*).

We introduce here an analytical threshold for determining *OT** on a case-by-case basis. Considering all data points in the LUT, Figure 8 shows variations of *OT** as a function of *RR_THRESH*. In general, more conservative detection thresholds (i.e., higher *RR_THRESH*) require an optically thicker cloud to enable detection of LTMP structure by way of the current algorithm. Also, relatively less absorbing and less forward scattering media (e.g., smaller effective radii and lower accompanying values of asymmetry parameter) require optically thicker clouds to enable appreciable penetration of the cloud media and discriminate phase at these levels. Both of these considerations are consistent with the general notion that the cloud, being an optically thick medium, must provide sufficient photon/particle interactions to produce an appreciable differential reflectance signal for confident detection. Based on the various sensitivity analyses described above, we settled on a threshold *RR_THRESH* of 1.2 as a conservative provisional value for benchmark testing of this algorithm. In future development, we will explore a dynamic threshold based on CDFs of reflectance ratios for a wide sampling of all-liquid clouds, similar in concept to the Bayesian approach of *Kummerow et al.* [1996, 2001]. Variations on detection performance as a function of specifying more aggressive/conservative values for this threshold are considered in the experiments presented in section 5 to follow.

4.5. Algorithm Flow

The LTMP detection algorithm operates on a pixel-by-pixel basis, following the procedure shown in Figure 9. The first determination is whether the pixel has predominately liquid phase at cloud top and cloud top temperatures below 273 K. This determination is made via conventional passive-based cloud top phase methods mentioned in section 2, but in principle could also be determined from an active sensor (e.g., CALIPSO or the future EarthCARE [*European Space Agency/Japan Aerospace Exploration Agency*, 2006] mission) or in situ (e.g., pilot reports along flight tracks that may then be used to characterize a regional cloud layer). In an operational setting, we would enlist the standard Level-2 products for this initial filtering step of the algorithm. Uncertainties in this upstream assignment will of course be inherited by the current algorithm.

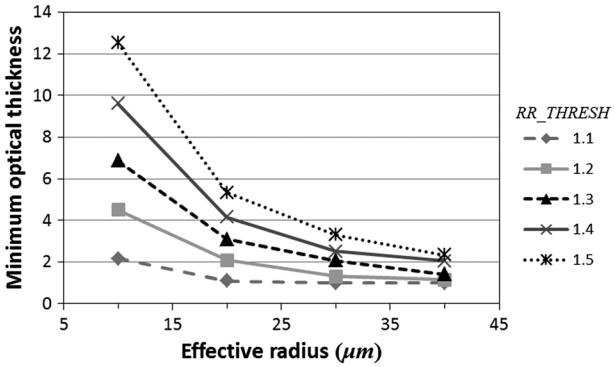

Figure 8. The minimum cloud optical thickness (*OT**) required for attempting LTMP detection via the current algorithm shown as a function of cloud particle effective radius and for various *RR_THRESH* thresholds ranging from aggressive (1.1) to conservative (1.5).

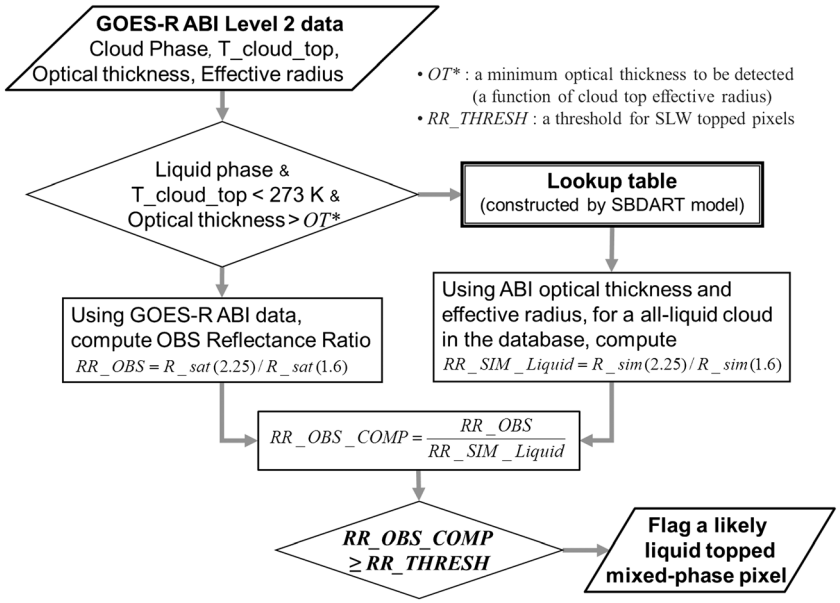

Figure 9. Flow chart of the LTMP cloud detection algorithm.

If the candidate pixel passes this initial filtering stage, it is then assessed for possible LTMP structure. Again, enlisting cloud optical property retrieval (Level-2) products provided from conventional retrievals, the visible optical thickness and cloud top effective radius are extracted. The pixel's optical thickness is then compared against the minimum optical thickness (*OT**), according to Figure 8, prior to proceeding with the algorithm.

For pixels satisfying the above criteria, we compute an observed reflectance ratio, *RR_OBS* (equation (5)). Using the retrieved cloud optical thickness, cloud top effective radius, and Sun/sensor geometry, we obtain from the LUTs the simulated reflectance ratio for an all-liquid cloud (*RR_SIM_Liquid*, extracted from the *RR_SIM_Mix* LUTs for the case of $\tau_{\_total} = \tau_{\_liquid}$ as mentioned above). Following equation (4), we then compute *RR_OBS_COMP*. If the value of *RR_OBS_COMP* is greater than or equal to our conservatively selected detection threshold, *RR_THRESH*, then the pixel is flagged as LTMP, and we proceed on to the next valid pixel in the scene. This process is repeated until all pixels in the image have been evaluated.

5. Observing System Simulation Experiments

Whereas the idealized scenarios suggest a potential useful signal will reside in the future GOES-R ABI measurements of LTMP clouds is important to evaluate the performance of the algorithm on more realistic conditions. The Visible/Infrared Imager/Radiometer Suite (VIIRS) on board the low-Earth-orbiting Suomi National Polar-orbiting Partnership (NPP) satellite [e.g., *Lee et al.*, 2010] also contains 1.61 and 2.25 μm bands (M10 and M11, respectively), which can be applied to the current algorithm. At the time of this development, no field campaigns providing suitable in situ cloud phase profile information colocated to VIIRS overpasses (e.g., from an aircraft campaign) were available for full validation. To examine algorithm performance quantitatively and in a controlled environment (where the presence of the LTMP structure is known a priori), we generated simulated GOES-R ABI satellite data using radiative transfer and numerical model output. This section describes the formulation and results of this exercise.

5.1. Experiment Setup

To simulate the ABI infrared brightness temperature and SIR reflectance measurements used in the cloud top phase and LTMP detection schemes, we utilized the Community Radiative Transfer Model (CRTM; version 2.0.5) developed at the Joint Center for Satellite Data Assimilation [*Han et al.*, 2007; *Weng*, 2007; *Chen et al.*, 2011]. The CRTM represents more than 100 sensors and often is used as a basis for simulating future satellite instruments. It was assumed for these simulations that the satellite was located at the current GOES-E

position (i.e., over the equator at 135°W), and corresponding solar/satellite viewing geometry data over the case study domains were computed.

Environmental state fields from the Weather Research and Forecasting (WRF) model [*Gallus and Bresch*, 2006] were used as input to the CRTM. Temperature, pressure, water vapor, hydrometeor mixing ratios, and surface information from the numerical model were used as input in order to simulate GOES-R ABI observations. The Advanced Research WRF dynamic core (version 3.4.1 released on 16 August 2012; see http://www.wrf-model.org) was run in a one-way nesting configuration of 27 km (domain 1), 9 km (domain 2), and 3 km (domain 3) grid spacing with 51 vertical levels. The runs employed the National Severe Storms Laboratory (NSSL) two-moment cloud microphysics scheme [*Mansell et al*., 2010], Yonsei University planetary boundary layer scheme [*Hong et al*., 2006], a simple cloud-interactive radiation scheme [*Dudhia*, 1989], and the Rapid Radiative Transfer Model longwave radiation scheme [*Mlawer et al*., 1997]. The Kain-Fritsch convective scheme [*Kain and Fritsch*, 1990, 1993] was used for domains 1 and 2. The National Center for Environmental Prediction Global Forecast System model output (0.5°) was used for initialization and lateral boundary condition information.

Two cases were considered here, based on the CLEX-10 Canadian CloudSat/CALIPSO Validation Programme joint field campaign (C3VP) [*Hudak et al*., 2007], where targeted observations of real-world clouds having LTMP structures were made from airborne and satellite sensors. More details for each case during the field campaign can be found in *Noh et al*. [2011], but they are summarized briefly here. In the 5 November 2006 case study, a warm front moved over Southern Ontario overnight and left behind a large area of midlevel. Altocumulus clouds were observed at a field program ground site (about 80 km north of Toronto, Canada) continuously for more than 10 h. The aircraft flying through the altocumulus layer around 1830 UTC revealed an LTMP structure, and CALIPSO [*Winker et al*., 2009] confirmed the presence of supercooled liquid water at cloud top (an in situ example of these mixed-phase clouds is shown in the Figure 1 (middle)). The 25 February 2007 case involves a midlatitude cyclone over the central U.S., which moved slowly toward the northeast and toward southern Ontario. This system produced a large area of midlevel cloud cover (mainly altostratus) which was sampled by various aircraft and satellite assets involved in the campaign. Although detailed verifications of the WRF model simulations with the NSSL two-moment microphysics scheme for these two cases are beyond the scope of this study, qualitatively, they produced realistic LTMP structured clouds in the target domain that were consistent to first order with field program observations and were thus deemed suitable for the purpose of evaluating our detection algorithm upon nonidealized structures.

The simulations for the two CLEX-10/C3VP wintertime mixed-phase cloud cases were integrated for 36 h starting from 1200 UTC initializations on 4 November 2006 and 1200 UTC on 24 February 2007, respectively. In these simulations, cloudy-sky model grid columns were identified as having column-integrated water paths exceeding 1.0 g/m^2 [*Noh et al*., 2013]. For reference, typical water paths for marine stratocumulus are ~100 g/m^2 [e.g., *Wood and Taylor*, 2001]. Effective radii for modeled cloud hydrometeors were calculated using the mixing ratio of each species (cloud water, ice, rain, snow, graupel, and hail) and number concentrations [*Mitchell*, 2002; *Otkin et al*., 2009], and only averaged effective radii for cloud liquid and ice particles down to visible optical thickness of 10.0 were considered (based on a sensitivity analyses of asymptotic reflectance versus cloud optical thickness at 1.61 μm and 2.25 μm, details not shown here). Cloud top temperatures were provided from simulated brightness temperatures at 10.35 μm. Cloud top phase was identified following the approach of *Pavolonis et al*. [2005], using brightness temperatures simulated by the CRTM at 8.5 μm and 11.2 μm for pixels with optical thickness (with respect to 0.64 μm wavelength) greater than 1.0, replicating the method applied to MODIS data.

5.2. Results

For each case study (1830 UTC on 5 November 2006 and 25 February 2007, hereafter, the 2006 and 2007 cases, respectively), we applied our algorithm to the CRTM-simulated GOES-R ABI observations according to the flow chart of Figure 9. The algorithm was applied to any identified supercooled liquid-topped clouds having optical thicknesses greater than the minimum OT^* values (as shown in Figure 8). Figure 10 shows examples of the CRTM-simulated brightness temperatures at 10.35 μm, along with arbitrarily defined vertical cross sections through the simulated cloudy scenes. In the 2007 case, the layer below the cloud top liquid is predominantly mixed phase as opposed to pristine ice. The CRTM is not forced to produce the

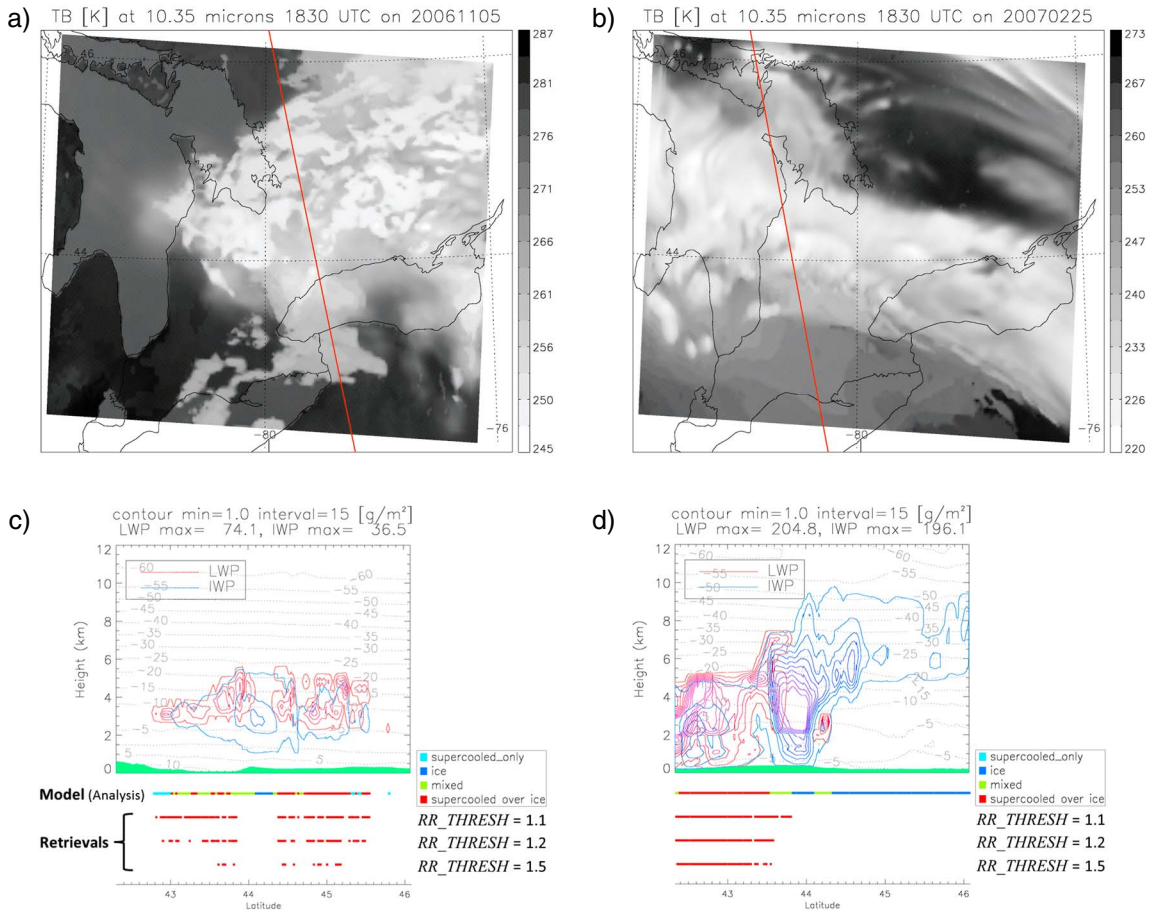

Figure 10. CRTM-simulated brightness temperatures for GOES-R ABI 10.35 μm using WRF model output for the (a) 05 November 2006 and (b) 25 February 2007 cases. (c and d) Cross section of liquid (blue) and ice (red) water contents with temperature contours (black dashed, in °C) from model simulations, extracted along the red lines shown in Figures 10a and 10b. Shown below these cross sections are the analyzed (truth) and the corresponding detection results shown for various *RR_THRESH*.

idealized case of a pristine liquid atop pristine ice phase, and in nature we may not expect such purely stratified conditions but instead a condition of either ice or mixed phase below the liquid-top layer. Positive detection of LTMP for this case underscores an important point: the current algorithm may be able to detect the *presence* of the below-cloud top ice phase, but it cannot provide insight on whether that phase existed in a pristine state or is possibly mixed phase. Detection performance based on varying *RR_THRESH* values of 1.1, 1.2, and 1.5 are shown. These cross sections reveal LTMP structures of the kind observed during the CLEX-10/C3VP campaign and targeted by the current algorithm.

Expanding to domain-wide spatial analysis, Figures 11 and 12 show the detection performance for each case study as a function of *RR_THRESH*. Cloud phase for the model analysis showing the actual distribution of LTMP structures are also shown in these plots for reference. The subset of clouds determined to be all supercooled liquid water are shown in cyan colors, while clouds determined as possibly LTMP are shown in red. Qualitatively, the patterns of LTMP cloud pixels flagged are similar to the "true" distribution, although some notable differences warrant examination. Notable areas of missed detections occur for the 2006 case, while some areas in the 2007 case (around (83° W, 42.5° N) and (81° W, 43° N)) contain false alarms. As *RR_THRESH* increases, the number of detected pixels decreases.

In an attempt to provide a more quantitative assessment of algorithm performance, we applied a simple statistical analysis following *Wilks* [1995]. The performance metrics of Hit Rate (HR; a measure of correct detection or correct nondetection of LTMP), Threat Score (TS; a measure of correct detection of LTMP for only the subset of clouds that were indeed fact LTMP), Probability of Detection (POD; the ratio of correction

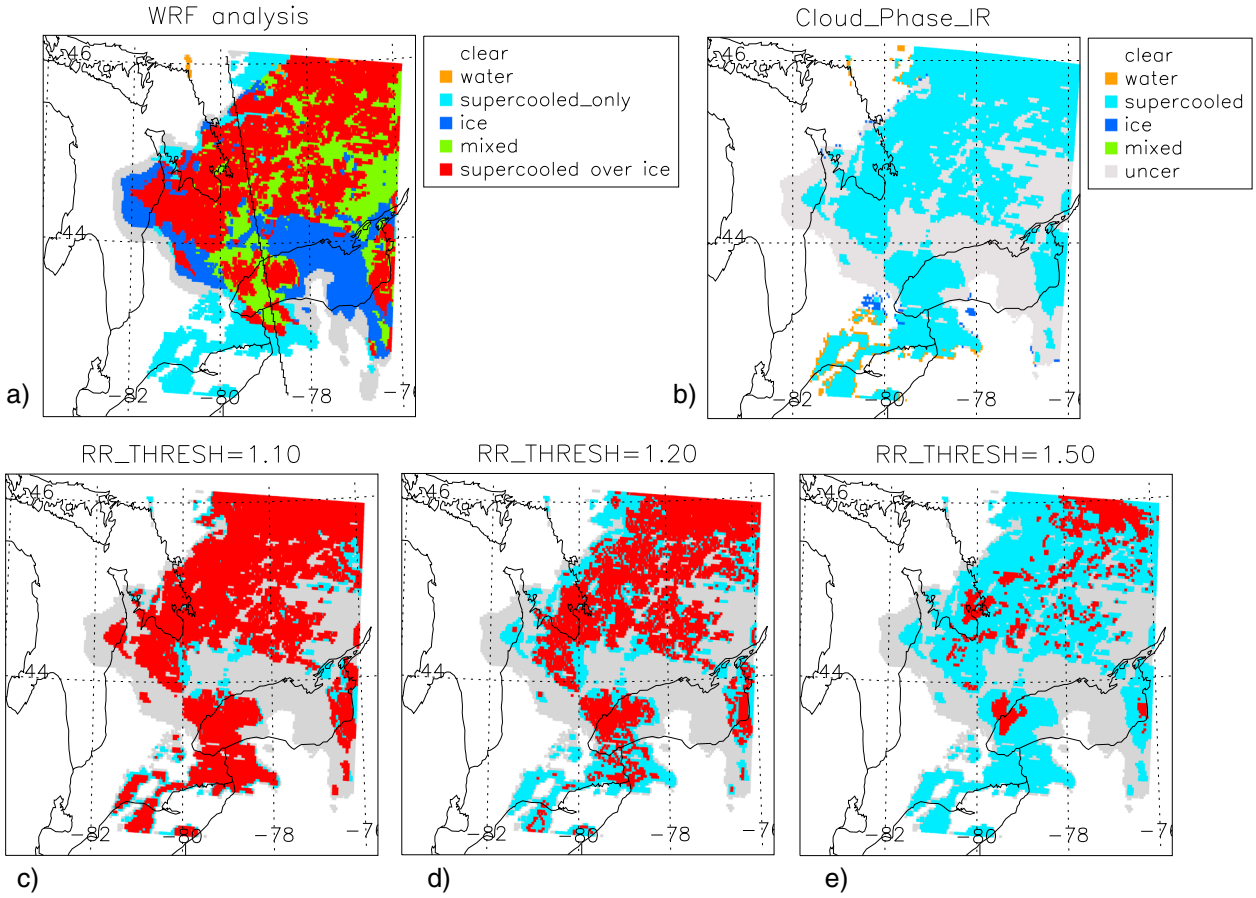

Figure 11. Detection algorithm performance test for the 5 November 2006 case: (a) WRF model cloud phase analysis for cloudy grid points, (b) cloud top phase retrieval obtained from GOES-R ABI synthetic brightness temperatures at 8.5 μm and 11.2 μm, and (c–e) results of the LTMP detection algorithm applied to the water phase pixels of Figure 11b, with LTMP clouds in red, supercooled liquid only in cyan, and unclassified clouds in gray, shown for various *RR_THRESH*.

detections to the total number of clouds considered), and False Alarm Rate (FAR; the ratio of missed detections to the total number of clouds considered) are expressed as

$$\mathrm{HR} = (\mathrm{A}+\mathrm{D})\Big/(\mathrm{A}+\mathrm{B}+\mathrm{C}+\mathrm{D}), \quad \mathrm{TS} = \mathrm{A}\Big/(\mathrm{A}+\mathrm{B}+\mathrm{C})$$
$$\mathrm{POD} = \mathrm{A}\Big/(\mathrm{A}+\mathrm{C}), \quad \mathrm{FAR} = \mathrm{B}\Big/(\mathrm{A}+\mathrm{B}) \tag{6}$$

where terms A, B, C, and D are defined in Table 1. Here the analysis is based only on the supercooled liquid water (SLW) clouds encountered in the scene. Table 2 shows the results of this analysis applied to the two case studies considered here. In both cases, the true fraction of LTMP clouds was about 80% (consistent with the CDF-based sensitivity studies discussed above), but the correct detection of these clouds varies with algorithmic threshold *RR_THRESH*. As expected, for lower *RR_THRESH* (and more aggressive) thresholds, higher HR and POD values are attained, but this comes at the expense of higher FAR. Selecting higher *RR_THRESH* (and thus more conservative) thresholds will lower the FAR but in so doing can also reduce the HR scores—an effect seen in the 2006 case. Interestingly, higher values of *RR_THRESH* served to slightly improve the HR scores in the 2007 case, although the difference is not significant above a certain value of *RR_THRESH* (a value of 1.2 was used here) and the TS scores do not vary significantly. Figure 10, while only a cross section, provides some insight on statistics behavior. Depending on the distribution and magnitude of the reflectance ratio signals, increasing the detection threshold can result in significant loss of detection (the 2006 case), or else a favorable removal of false alarms (the 2007 case). An important distinction between the 2006 and 2007 cases is that the latter features optically thicker clouds and inherently stronger reflectance ratio signals.

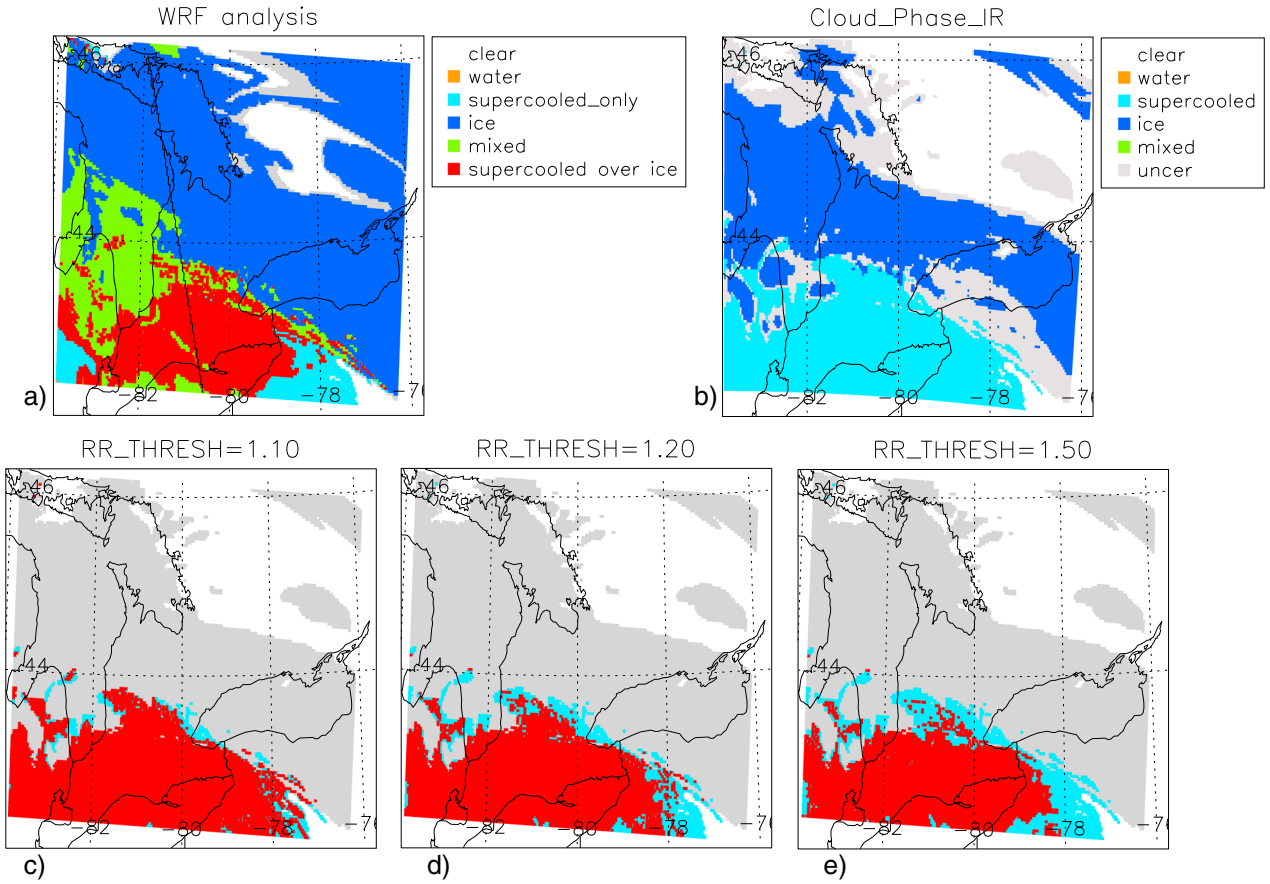

Figure 12. Same as Figure 11 but for the 25 February 2007 case.

Despite the attempts to present realistic case studies to exercise the algorithm, clearly our definition of "truth" in the simulated data set (i.e., what is determined as constituting LTMP) plays an important role in the performance statistics. We attempt to adhere to the general rules of an optically thick liquid top, with the presence of an ice phase (either pristine or mixed) below. It is worth emphasizing that application of the TIR-based cloud top phase algorithm (considered a priori information to the current algorithm) to these model data provides the expected result and that the LTMP algorithm applied to this subset of clouds appears to provide discrimination between all-liquid and LTMP situations. With that said, even though the simulated cloud liquid/ice mixtures (as seen in Figure 10) are far more complex than the idealized two-layer cloud structures upon which the LUTs are based, it is expected that real-world clouds will exhibit similar if not even more complex structures. Thus, performance based on these simulated case studies offer only a glimpse into expected performance. It should also be noted that the cases shown in Figures 11 and 12 contain a large fraction (>80% as shown in Table 2) of the target LTMP structure, meaning that opportunities for false alarms are inherently reduced. A more rigorous validation of the current algorithm under a broader variety of conditions, and including in situ observations, will be required to help identify and characterize in a comprehensive way the actual limits of algorithm.

Table 1. Strategy for Statistical Analyses of C3VP Case Studies Shown in Figures 11 and 12

		Observation (Proxy From WRF Model Simulations)	
		SLW Over Ice	SLW Only
Detection algorithm	SLW over ice SLW only	**A**: "SLW over ice" hit **C**: SLW over ice miss	**B**: SLW over ice false alarm **D**: "SLW only" hit

Table 2. Performance Statistics for the Case Studies Shown in Figures 11 and 12[a]

Case Date	True SLW Over Ice Pixels (%)	*RR_THRESH*	Detected SLW Over Ice Pixels (%)	HR	TS	POD	FAR
5 Nov 2006	80.942	1.1	80.484	0.711	0.696	0.838	0.196
		1.2	55.021	0.691	0.627	0.660	0.074
		1.5	18.578	0.405	0.248	0.249	0.013
25 Feb 2007	81.920	1.1	89.262	0.789	0.779	0.961	0.195
		1.2	80.260	0.800	0.782	0.928	0.167
		1.5	71.181	0.803	0.775	0.873	0.127

[a]The percentage of LTMP clouds (columns 2 and 4) is with respect to all supercooled liquid-topped clouds detected in the scene.

6. Case Study Analysis

As a preliminary form of validation against actual observations, we considered a case study offering near-simultaneous colocation of NPP VIIRS, CloudSat, and CALIPSO, all occurring in close proximity to the Department of Energy Atmospheric Radiation Measurement (ARM) Climate Research Facility on the North Slope of Alaska (NSA) at Barrow (71.323°N, 156.609°W) [*Verlinde et al*., 2007]. Detailed information about the NSA site is available online at http://www.arm.gov/sites/nsa. The site includes an upward pointing High Spectral Resolution Lidar (HSRL) [*Shipley et al*., 1983] offering polarimetric-based phase determination [e.g., *Sassen*, 2005; *Verlinde et al*., 2007] similar in capacity to CALIPSO but from the subliquid-top vantage point. Since CALIPSO attenuates fully in the LTMP clouds and CloudSat does not offer direct phase determination, the HSRL lidar is particularly useful in confirming the LTMP condition.

Figure 13 summarizes the satellite observations (Suomi NPP VIIRS, CloudSat, and CALIPSO, which share a common orbital plane) enlisted for this evaluation. The strong backscatter and sharp attenuation in CALIPSO is characteristic of liquid-topped clouds, while CloudSat's detection of subcloud top returns is consistent with larger ice crystals in the LTMP structure. On 27 June 2013, the Suomi NPP and NASA A-Train ground tracks were within in close orbital alignment. This colocation, which occurs every 2–3 days as the lower altitude A-Train constellation "laps" Suomi NPP, met these criteria between 27 June 2230 UTC and 28 June 0309 UTC. Near the beginning of this colocation, the satellite ground tracks passed in very close proximity to the ARM NSA site. This enabled a multiobserving system view of a complex cloud field which included supercooled and mixed-phase cloud tops, along with VIIRS data that permit application of our algorithm. In terms of both available sensors and relevant meteorology, the alignment was regarded as extremely serendipitous.

The time series of upward pointing HSRL observations (Figure 14), collected at the ARM NSA site within 30 min of the colocated satellite overpasses, shows the classic structure of a LTMP cloud. We note that in the case of the upward pointing HSRL, just as in the case of the downward pointing CALIPSO lidar, the liquid phase layer attenuates the beam completely. Here we are left with a truncated view of the atmospheric column, capped by the liquid layer base. This base is identified near 2.8–3.0 km, with accompanying strong lidar backscatter and low depolarization ratios (indicative of spherical liquid droplets). Combining this information with the CALIPSO observations, we may deduce that the liquid layer of the LTMP cloud was roughly 1 km thick. There is a period of precipitating ice (indicated by higher values of lidar depolarization ratio) between 2240 and 2250 UTC. This subcloud top information to complement the cloud top liquid phase is the critical missing piece of information which cannot be supplied by CALIPSO and bolsters confidence in lieu of in situ observations. The observations are used simply to confirm the presence of LTMP clouds in the immediate vicinity of the AMR NSA site at the time of the satellite overpasses.

We proceeded to apply the LTMP detection algorithm to the VIIRS M10 (1.61 μm) and M11 (2.25 μm) bands, along with information about cloud type, optical depth, particle size retrieved from VIIRS (standard Level-2 products), and the Sun/sensor geometry information from the VIIRS geolocation file. The algorithm was run on a variety of normalized reflectance ratio thresholds, and traces of these detection results were extracted along the CloudSat/CALIPSO ground track, similar to the procedure followed in the model simulation case studies.

The results of this analysis are shown in Figure 15. The scene was prescreened to remove cases of cloud top pristine ice phase, per assumptions, and protocols of the algorithm. Among those supercooled liquid/mixed clouds remaining, there were many areas where the algorithm flagged the presence of a LTMP structure. Even at the higher (more conservative) reflectance ratio threshold of 1.5, the algorithm retains

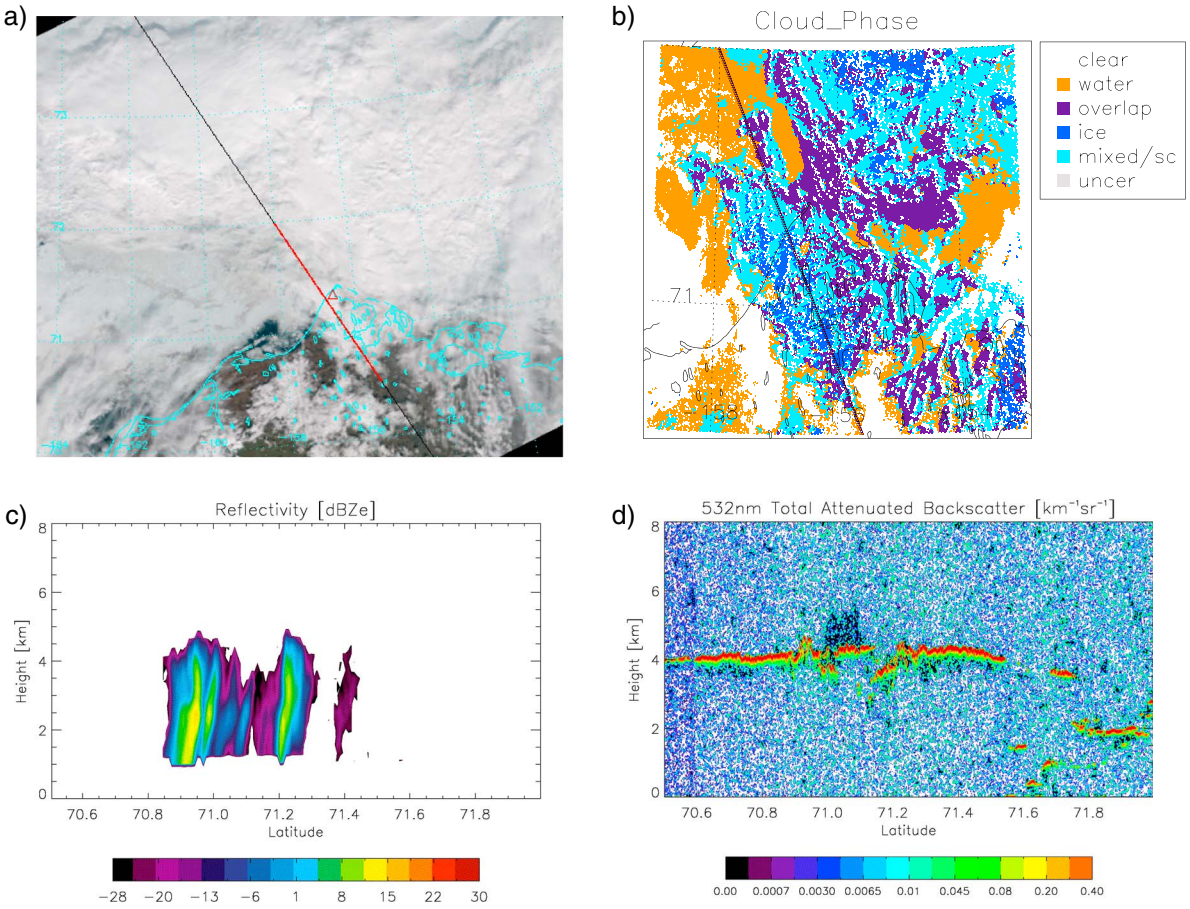

Figure 13. Space and time colocated satellite observations over the ARM NSA area at 22:30–22:35 UTC on 27 June 2013, (a) S-NPP VIIRS true color image with the CloudSat/CALIPSO overpass (line; satellites moving from lower right to upper left on this ascending node) and the nearby ARM NSA location (triangle), (b) VIIRS cloud phase showing a complex distribution of cloud types across the region (with CloudSat/CALIPSO ground track overlaid as a black line), (c) CloudSat W-band radar reflectivity, and (d) CALIPSO 532 nm lidar total attenuated backscatter along the red-highlighted portion of ground track shown in Figure 13a.

significant patches of LTMP designation, including a patch that is in very close proximity to the CloudSat/CALIPSO/HSRL joint observations. Here detections of LTMP remain affirmative between 70.8° and 71.4° latitude along the ground track. Cross referencing this information with the CloudSat (and HSRL depolarization ratio) observations shown suggests that the detection coincides with the shafts of precipitating ice—ostensibly confirming that the algorithm is functioning as predicted.

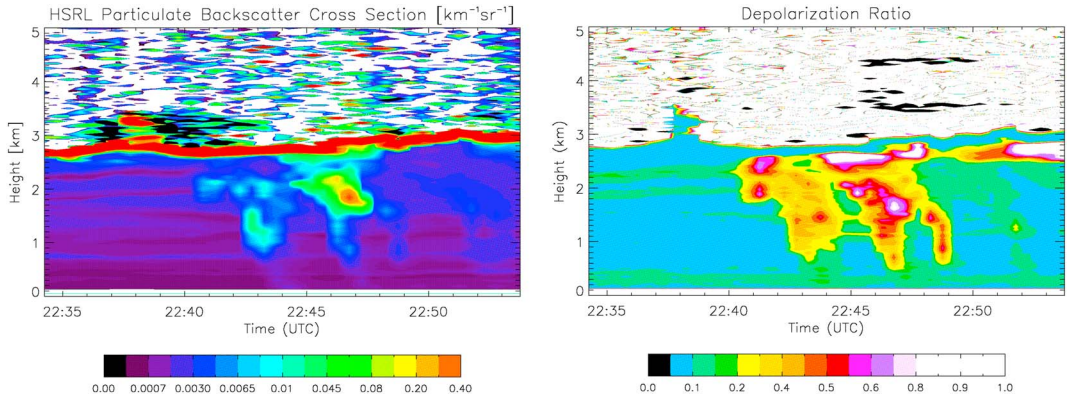

Figure 14. Time series of (left) attenuated backscatter and (right) depolarization ratio observed from the upward pointing ARM NSA HSRL instrument for the case study on 27 June 2013.

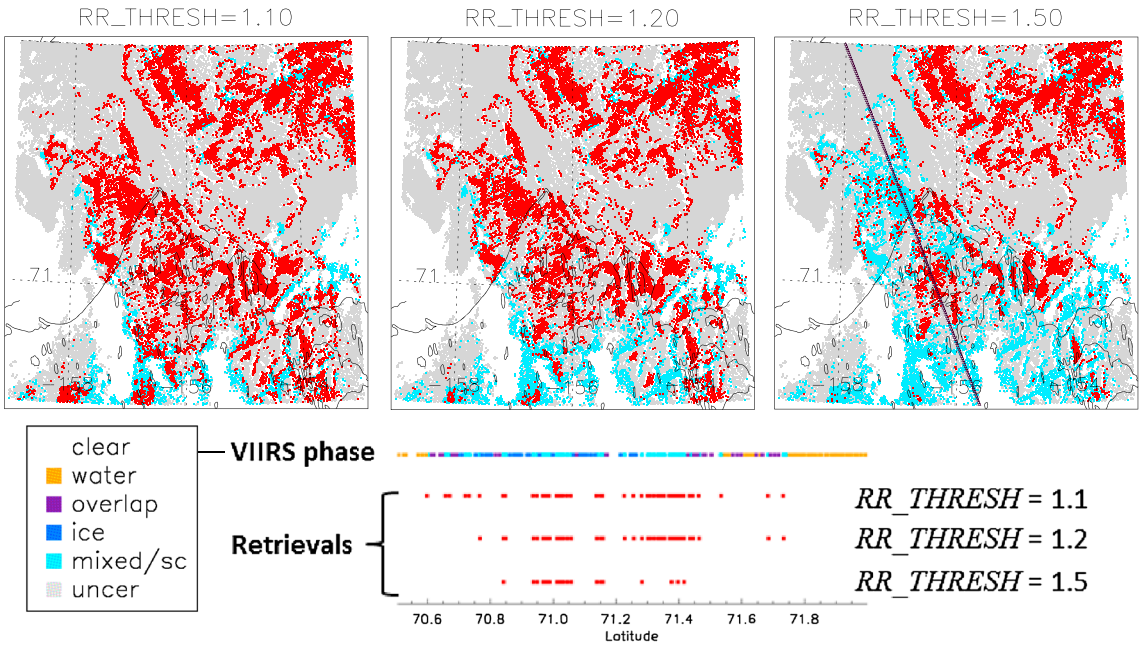

Figure 15. Detection algorithm performance test with S-NPP VIIRS measurements for the 27 June 2013 case. LTMP detection algorithm applied to the VIIRS supercooled/mixed-phase pixels for various *RR_THRESH* as shown, with positive detection LTMP clouds in red, supercooled liquid only (negative detection) in cyan and unconsidered clouds in gray. Shown below are cross sections of cloud phase and the corresponding detection results (as in Figure 10) extracted along the CloudSat/CALIPSO ground track (black line in the top right panel).

We acknowledge that this ARM/NSA case study analysis by no means represents a vigorous validation of the current algorithm. The scene is very complex and replete with LTMP detections. What the case does provide is an additional form of comparison beyond the idealized and NWP-based methods and perhaps the motivation to continue pursuit of this algorithm's development, refinement, and evaluation on future measurement campaigns that offer an in situ component.

7. Discussion and Conclusion

The physical basis for an algorithm targeting the daytime detection of clouds exhibiting liquid top and mixed phase or pristine ice below cloud top has been presented. It begins with upstream information about cloud mask, cloud top phase, cloud top particle size (effective radius), and cloud optical thickness. The algorithm takes advantage of differential optical properties of liquid and ice phase cloud particles using SIR bands whose weighting functions peak below cloud top and below levels of sensitivity for conventional cloud top phase discrimination techniques, thus enabling probing of the optically thick media. The algorithm holds promise for assisting researchers in inferring the distribution and nature of these clouds, providing further insight to their formation mechanisms, and there also exist practical applications with respect to aviation and airframe icing concerns.

To develop the algorithm, a simple two-layer cloud model was assumed, composed of variable fractions of liquid and ice phase. LUTs based on SBDART radiative transfer calculations for this idealized scenario span the practical solution space of cloud optical thickness, cloud top effective radius, and Sun/sensor geometry. The departure of reflectance ratios between the observed cloud and an idealized all-liquid cloud having the same bulk properties (total cloud optical depth, cloud top effective particle size, under the assumption of similar Sun/sensor geometry) as those retrieved is used to gauge the likelihood of the LTMP condition based on a conservatively selected and cloud property-dependent threshold value. The outcomes of this algorithm are a flag for positive identification of LTMP and as a by-product an estimate of the liquid-top cloud optical thickness.

Observing system experiments based on WRF simulations of LTMP cloud systems reveal both capabilities and limitations of the current algorithm. Whereas positive detection of some LTMP clouds and correct exclusion of pure liquid phase clouds was achieved, performance was tied heavily to the reflectance ratio threshold

selected. In addition, the algorithm does not appear to provide insight on whether the subcloud top layer is pure ice versus mixed phase—the presence of sufficient ice phase within the subcloud top optical thickness region of SIR band sensitivity will trigger detection. An imposed threshold on the reflectance ratio of 1.2 was found to strike the best compromise between detection and avoidance of false alarms, offering detection of roughly 60–80% of LTMP cases encountered in the simulation experiments and false alarm rates less than 0.2. An observational case study of clouds near the ARM NSA site lends further credence to the technique's ability to identify the LTMP structure at conservative thresholds.

This algorithm was designed with an eye toward applications on the future ABI sensors of the next-generation GOES-R series and Japan Meteorological Agency Himawari-8/9 (Advanced Himawari Imager (AHI)) satellites. Both the ABI and AHI will offer 1.58–1.64 μm (1.61 μm nominal band center) and 2.225–2.275 μm (2.25 μm) narrow spectral bands, useful for the current approach. As shown in the case study, it is also applicable to selected polar-orbiting sensors such as VIIRS, but not directly applicable to MODIS since its 2.13 μm channel (Band 7) does not provide a reversal of liquid/ice absorption properties which is at the heart of the technique (see Figure 2). We look toward the geostationary application as supplying the critical temporal component for understanding the evolution of LTMP structure. However, a pairing of 2.25/2.13 μm may, in fact, provide superior performance to the 2.25/1.61 μm pairing described here. In this regard, hyperspectral sensors providing spectral coverage in SIR could be used to produce "superbands" from selected subsets of the spectrum providing optimal phase sensitivity.

As with any algorithm developed on idealized assumptions, there exist a host of theoretical and practical limitations and several areas for potential improvement. Foremost among them, real clouds will not exhibit the pristine bifurcation of phase that is assumed in the simulations—the subcloud top layer may be a complex mixed-phase distribution with a variety of particle sizes and habits. The current technique is not equipped to make a detailed assessment, but the bulk absorption properties offer a chance of inferring the presence of this mixed phase when the observed reflectance ratio exceeds critical thresholds. Given its usage of solar reflectance information, the daytime-only nature of the algorithm precludes its ability to provide diurnal information and eliminates its utility during the polar winter (where many of the LTMP clouds of interest may reside). In terms of basic performance, while the WRF-based simulations and ARM/NSA case study are promising, we anticipate that some real-world LTMP clouds may hold additional challenges to detection (e.g., too optically thin).

The plane-parallel assumptions of the simulated reflectance ratios may fail when confronted with subpixel heterogeneity, particularly over land surfaces. Higher spatial resolution observations can mitigate these issues in part, but for GOES-R and its 2 km IR pixels this will indeed be an issue. Our plan when implementing this on GOES-R data is to examine the 0.5 km visible band as a way of assessing subpixel heterogeneity and potentially filtering these pixels from consideration, and initial demonstrations will be over water pixels exclusively. Being a passive measurement technique, this algorithm is not applicable to cases of overriding cirrus. Finally, if the cloud top phase detection algorithm (assumed here as a starting point for application of the LTMP detection algorithm) flags mixed-phase top clouds as "liquid top," then this could lead to false detections of LTMP in the current algorithm. It is seen in Figure 5 that the reflectance ratio signal will continue to increase with decreasing cloud top liquid phase, so applying our current algorithm to such clouds could yield detections of LTMP when, in fact, these clouds may not have a pure liquid-top phase. As such, proper quality control on the upstream cloud top phase retrieval would be an essential first step here.

In future work, the algorithm will be tested and validated for more cases to improve quantitative uncertainty estimates and refined to implement dynamically specified reflectance ratio detection thresholds. Specifically, for a given Sun/viewing geometry and set of retrieved cloud optical properties, a critical *RR_THRESH* may be derived as opposed to a conservatively selected CDF-based value. Additional constraints using various channel combinations and potentially the incorporation of lidar depolarization and backscatter intensity information (which provides phase discrimination) [e.g., *Hu et al.*, 2010] will be also examined in an effort to delineate more clearly between liquid-top and mixed-phase top clouds. Validation against in situ observations will be of prime importance to building confidence in the algorithm and refining detection thresholds. Here VIIRS (and the future AHI and ABI sensors) matchups with CALIPSO and/or the future EarthCARE active sensors, together with coordinated underflights by instrumented aircraft (anticipated to coincide with EarthCARE) will be examined.

Acknowledgments
This work was supported by the Naval Research Laboratory through contracts N00173-10-C-2003 and N00173-14-1-G902, the Oceanographer of the Navy through the Program Executive Office C4I/PMW-120 under program element PE-0603207 N, and the DoD Center for Geosciences/Atmospheric Research at Colorado State University under Cooperative Agreement W911NF-06-2-0015 with the Army Research Laboratory. The views, opinions, and findings contained in this report are those of the authors and should not be construed as an official National Oceanic and Atmospheric Administration or U.S. Government position, policy, or decision.

References

Baran, A. J., V. N. Shcherbakov, B. A. Baker, J. F. Gayet, and R. P. Lawson (2005), On the scattering phase function of non-symmetric ice-crystals, *Q. J. R. Meteorol. Soc.*, *131*, 2609–2616.

Baum, B. A., P. F. Soulen, K. I. Strabala, M. D. King, S. A. Ackerman, W. P. Menzel, and P. Yang (2000), Remote sensing of cloud properties using MODIS Airborne Simulator imagery during SUCCESS. II. Cloud thermodynamic phase, *J. Geophys. Res.*, *105*, 11,781–11,792, doi:10.1029/1999JD901090.

Beesley, J. A., and R. E. Moritz (1999), Toward an explanation of the annual cycle of cloudiness over the Arctic Ocean, *J. Clim.*, *12*, 395–415.

Bergeron, T. (1935), On the physics of clouds and precipitation, *Proces Verbaux de l'Association de Météorologie*, Lisbon, Portugal, International Union of Geodesy and Geophysics, 156–178.

Carey, L. D., J. Niu, P. Yang, J. A. Kankiewicz, V. E. Larson, and T. H. Vonder Haar (2008), The vertical profile of liquid and ice water content in mid-latitude mixed-phase altocumulus clouds, *J. Appl. Meteor. Climatol.*, *47*, 2487–2495.

Chang, F.-L., and Z. Li (2002), Estimating the vertical variation of cloud droplet effective radius using multispectral near-infrared satellite measurements, *J. Geophys. Res.*, *107*(D15), doi:10.1029/2001JD000766.

Chang, F.-L., and Z. Li (2003), Retrieving vertical profiles of water-cloud droplet effective radius: Algorithm modification and preliminary application, *J. Geophys. Res.*, *108*(D24), 4763, doi:10.1029/2003JD003906.

Chen, Y., Y. Han, Q. Liu, P. Van Delst, and F. Weng (2011), Community radiative transfer model for stratospheric sounding unit, *J. Atmos. Oceanic Technol.*, *28*, 767–778, doi:10.1175/2010JTECHA1509.1.

Civil Aviation Authority (2000), *Aircraft Icing Handbook*, 1st ed., New Zealand. [Available at http://www.caa.govt.nz/safety_info/gaps/aircraft_icing_handbook.pdf.]

Cober, S. G., G. A. Isaac, and J. W. Strapp (1995), Aircraft icing measurements in east coast winter storms, *J. Appl. Meteorol.*, *34*, 88–100.

Curry, J. A., W. B. Rossow, D. Randall, and J. L. Schramm (1996), Overview of Arctic cloud and radiation characteristics, *J. Clim.*, *9*, 1731–1764.

Dudhia, J. (1989), Numerical study of convection observed during the winter monsoon experiment using a mesoscale two-dimensional model, *J. Atmos. Sci.*, *46*, 3077–3107.

Ellrod, G. P. (1996), The use of GOES-8 multispectral imagery for the detection of aircraft icing regions, Preprints, paper presented at Eighth Conference on Satellite Meteorology and Oceanography, Am. Meteorol. Soc., Atlanta, Ga.

Ellrod, G. P., and A. A. Bailey (2007), Assessment of aircraft icing potential and maximum icing altitude from geostationary meteorological satellite data, *Weather Forecasting*, *22*, 160–174.

European Space Agency/Japan Aerospace Exploration Agency (2006), EarthCARE mission requirement document version 5, EC-RS-ESA-SY-012. [Available at http://esamultimedia.esa.int/docs/EarthObservation/EarthCARE_MRD_v5.pdf.]

Findeisen, W. (1938), Kolloid-meteorologische vorgänge bei Neiderschlags-Bildung, *Meteor. Z.*, *55*, 121–133.

Fleishauer, R. P., V. E. Larson, and T. H. Voner Haar (2002), Observed microphysical structure of mid-level, mixed-phase clouds, *J. Atmos. Sci.*, *59*, 1779–1804.

Fowler, L. D., D. A. Randall, and S. A. Rutledge (1996), Liquid and ice cloud microphysics in the CSU general circulation model. Part I: Model description and simulated microphysical processes, *J. Clim.*, *9*, 489–529.

Gallus, W. A., and J. F. Bresch (2006), Comparison of impacts of WRF dynamic core, physics package, and initial conditions on warm season rainfall forecasts, *Mon. Weather Rev.*, *134*, 2632–2641.

Hallett, J., and S. C. Mossop (1974), Production of secondary ice particles during the riming process, *Nature*, *249*, 26–28.

Han, Y., F. Weng, Q. Liu, and P. van Delst (2007), A fast radiative transfer model for SSMIS upper atmosphere sounding channels, *J. Geophys. Res.*, *112*, D11121, doi:10.1029/2006JD008208.

Harrington, J. Y., T. Reisin, W. R. Cotton, and S. M. Kreidenweis (1999), Cloud resolving simulations of Arctic stratus. Part II: Transition-season clouds, *J. Atmos. Res.*, *51*, 45–75.

Hong, S.-Y., Y. Noh, and J. Dudhia (2006), A new vertical diffusion package with an explicit treatment of entrainment processes, *Mon. Weather Rev.*, *134*, 2318–2341.

Hu, Y., S. Rodier, K.-M. Xu, W. Sun, J. Huang, B. Lin, P. Zhai, and D. Josset (2010), Occurrence, liquid water content, and fraction of supercooled water clouds from combined CALIOP/IIR/MODIS measurements, *J. Geophys. Res.*, *115*, D00H34, doi:10.1029/2009JD012384.

Hu, Y.-X., and K. Stamnes (1993), An accurate parameterization of the radiative properties of water clouds suitable for use in climate models, *J. Clim.*, *6*(4), 728–742.

Hudak, D., H. Barker, K. Strawbridge, M. Wolde, A. Kankiewicz, and J. W. Strapp (2007), The Canadian Cloudsat CALIPSO Validation Project: Evaluation of sensitivity and sub-pixel variability of Cloudsat data products, Preprints, paper presented at 33rd Conference on Radar Meteorology, Cairns, Australia, 6–10 Aug.

Inoue, T., and S. A. Ackerman (2002), Radiative effects of various cloud types as classified by the split window technique over the eastern sub-tropical Pacific derived from collocated ERBE and AVHRR data, *J. Meteorol. Soc. Jpn.*, *80*(6), 1383–1394.

Kain, J. S., and J. M. Fritsch (1990), A one-dimensional entraining/detraining plume model and its application in convective parameterization, *J. Atmos. Sci.*, *47*, 2784–2802.

Kain, J. S., and J. M. Fritsch (1993), *Convective Parameterization for Mesoscale Models: The Kain-Fritsch Scheme. The Representation of Cumulus Convection in Numerical Models*, *Meteor. Monogr.*, vol. 24, pp. 165–170, Am. Meteorol. Soc., Boston.

King, N. J., and G. Vaughan (2012), Using passive remote sensing to retrieve the vertical variation of cloud droplet size in marine stratocumulus: An assessment of information content and the potential for improved retrievals from hyperspectral measurements, *J. Geophys. Res.*, *117*, D15206, doi:10.1029/2012JD017896.

Klein, S. A., et al. (2009), Intercomparison of model simulations of mixed-phase clouds observed during the ARM Mixed-Phase Arctic Cloud Experiment I: Single layer cloud, *Q. J. R. Meteorol. Soc.*, *135*(641), doi:10.1002/qj.416.

Kogan, Z. N., and Y. L. Kogan (2001), Parameterization of drop effective radius for drizzling marine stratocumulus, *J. Geophys. Res.*, *106*, 9757–9764, doi:10.1029/2001JD900041.

Kummerow, C., W. S. Olson, and L. Giglio (1996), A simplified scheme for obtaining precipitation and vertical hydrometeor profiles from passive microwave sensors, *IEEE Trans. Geosci. Remote Sens.*, *34*, 1213–1232.

Kummerow, C., Y. Hong, W. S. Olson, S. Yang, R. F. Adler, J. McCollum, R. Ferraro, G. Petty, D.-B. Shin, and T. T. Wilheit (2001), The evolution of the Goddard Profiling Algorithm (GPROF) for rainfall estimation from passive microwave sensors, *J. Appl. Meteorol.*, *40*, 1801–1820.

Lee, T. F., et al. (2010), NPOESS: Next-generation operational global Earth observations, *Bull. Am. Meteorol. Soc.*, *91*, 727–740.

Lee, T. F., F. J. Turk, and K. Richardson (1997), Stratus and fog products using GOES-8, -9, 3.9 p.m data, *Weather Forecasting*, *12*, 664–677.

Liu, X., S. J. Ghan, and S. Xie (2007), Evaluation of mixed-phase cloud microphysics parameterizations with the NCAR single column climate model (SCAM) and ARM observations, *2nd Quarter 2007 ARM Metric Rep.*, DOE/SC-ARM-P-07-006, 11 pp.

Mace, G. G., R. Marchand, and G. L. Stephens (2007), Global hydrometeor occurrence as observed by CloudSat: Initial observations from summer 2006, *Geophys. Res. Lett.*, *34*, L09808, doi:10.1029/2006GL029017.
Mansell, E. R., C. L. Ziegler, and E. C. Bruning (2010), Simulated electrification of a small thunderstorm with two-moment bulk microphysics, *J. Atmos. Sci.*, *67*, 171–194, doi:10.1175/2009JAS2965.1.
Mecikalski, J. R., et al. (2007), Aviation applications for satellite-based observations of cloud properties, convection initiation, in-flight icing, turbulence, and volcanic ash, *Bull. Am. Meteorol. Soc.*, *88*, 1589–1607.
Meehl, G. A., C. Covey, T. Delworth, M. Latif, B. McAvaney, J. F. Mitchell, R. J. Stouffer, and K. E. Taylor (2007), The WCRP CMIP3 multimodel dataset, *Bull. Am. Meteorol. Soc.*, *88*, 1383–1394.
Miller, S. D., G. L. Stephens, C. K. Drummond, A. K. Heidinger, and P. T. Partain (2000), A multisensor diagnostic cloud property retrieval scheme, *J. Geophys. Res.*, *105*(D15), 19,955–19,971, doi:10.1029/2000JD900273.
Miller, S. D., G. L. Stephens, and R. T. Austin (2001), GOES 10 cloud optical property retrievals in the context of vertically varying microphysics, *J. Geophys. Res.*, *106*(D16), 17,891–17,995.
Mitchell, D. L. (2002), Effective diameter in radiative transfer: General definition, applications, and limitations, *J. Atmos. Sci.*, *59*, 2330–2346.
Mlawer, E. J., S. Taubman, P. D. Brown, M. J. Iacono, and S. A. Clough (1997), Radiative transfer for inhomogeneous atmospheres: RRTM, a validated correlated-k model for the longwave, *J. Geophys. Res.*, *102*, 16,663–16,682, doi:10.1029/97JD00237.
Mossop, S. C., A. Ono, and E. R. Wishart (1970), Ice particles in maritime clouds near Tasmania, *Q. J. R. Meteorol. Soc.*, *96*, 487–508.
Nagao, T. M., K. Suzuki, and T. Y. Nakajima (2013), Interpretation of multiwavelength-retrieved droplet effective radii for warm water clouds in terms of in-cloud vertical inhomogeneity by using a spectral bin microphysics cloud model, *J. Atmos. Sci.*, *70*, 2376–2392.
Nakajima, T., and M. D. King (1990), Determination of the optical thickness and effective particle radius of clouds from reflected solar radiation measurements. Part I: Theory, *J. Atmos. Sci.*, *47*(15), 1878–1893.
Nakajima, T. Y., K. Suzuki, and G. L. Stephens (2010a), Droplet growth in warm water clouds observed by the A-Train. Part I: Sensitivity analysis of the MODIS-derived cloud droplet sizes, *J. Atmos. Sci.*, *67*, 1884–1896.
Nakajima, T. Y., K. Suzuki, and G. L. Stephens (2010b), Droplet growth in warm water clouds observed by the A-Train. Part II: A multi-sensor view, *J. Atmos. Sci.*, *67*, 1897–1907.
Niu, J., L. D. Carey, P. Yang, and T. H. Vonder Haar (2008), Optical properties of a vertically inhomogeneous mid-latitude mid-level mixed-phase altocumulus in the infrared, *Atmos. Res.*, *88*, 234–242.
Noh, Y. J., C. Seaman, T. H. Vonder Haar, D. R. Hudak, and P. Rodriguez (2011), Comparisons and analyses of wintertime mixed-phase clouds using satellite and aircraft observations, *J. Geophys. Res.*, *116*, D18207, doi:10.1029/2010JD015420.
Noh, Y. J., C. J. Seaman, T. H. Vonder Haar, and G. Liu (2013), In situ aircraft measurements of water content profiles in various midlatitude mixed-phase clouds, *J. Appl. Meteor. Climatol.*, *52*, D110202, doi:10.1175/JAMC-D-11-0202.1.
Otkin, J. A., T. J. Greenwald, J. Sieglaff, and H.-L. Huang (2009), Validation of a large-scale simulated brightness temperature dataset using SEVIRI satellite observations, *J. Appl. Meteor. Climatol.*, *48*, 1613–1626.
Ou, S. S. C., et al. (2009), Retrievals of mixed-phase cloud properties during the National Polar-Orbiting Operational Environmental Satellite System, *Appl. Optics*, *48*, 1452–1462.
Pavolonis, M. J. (2010), Advances in extracting cloud composition information from spaceborne infrared radiances—A robust alternative to brightness temperatures. Part I: Theory, *J. Appl. Meteor. Climatol.*, *49*, 1992–2012.
Pavolonis, M. J., A. K. Heidinger, and T. Uttal (2005), Daytime global cloud typing from AVHRR and VIIRS: Algorithm description, validation, and comparisons, *J. Appl. Meteorol.*, *44*, 804–826.
Pinto, J. O. (1998), Autumnal mixed-phase cloudy boundary layers in the Arctic, *J. Atmos. Sci.*, *55*, 2016–2038.
Platnick, S. (2000), Vertical photon transport in cloud remote sensing problems, *J. Geophys. Res.*, *105*, 22,919–22,935, doi:10.1029/2000JD900333.
Platnick, S., M. D. King, S. A. Ackerman, W. P. Menzel, B. A. Baum, J. C. Riedi, and R. A. Frey (2003), The MODIS cloud products: Algorithms and examples from Terra, *IEEE Trans. Geosci. Remote Sens.*, *41*(2), 459–473.
Rauber, R. M., and A. Tokay (1991), An explanation for the existence of supercooled water at the tops of cold clouds, *J. Atmos. Sci.*, *48*, 1005–1023.
Ricchiazzi, P., S. Yang, C. Gautier, and D. Sowle (1998), SBDART: A research and teaching software tool for plane parallel radiative transfer in the Earth's atmosphere, *Bull. Am. Meteorol. Soc.*, *79*, 2101–2114.
Sassen, K. (2005), Polarization in Lidar, in *Lidar: Range-Resolved Optical Remote Sensing of the Atmosphere*, chap. 2, edited by C. Weitkamp, pp. 19–42, Springer, New York.
Schmit, T. J., M. M. Gunshor, W. P. Menzel, J. J. Gurka, J. Li, and A. S. Bachmeier (2005), Introducing the next generation advanced baseline imager on GOES-R, *Bull. Am. Meteorol. Soc.*, *86*, 1079–1096.
Schneider, D., and M. Moneypenny (2002), The mesoscale seeder-feeder mechanism: Its forecast implications, *Nat. Wea. Digest*, *26*(12), 45–52.
Shipley, S. T., D. H. Tracy, E. W. Eloranta, J. T. Trauger, J. T. Sroga, F. L. Roesler, and J. A. Weinman (1983), A High Spectral Resolution Lidar to measure optical scattering properties of atmospheric aerosols, Part I: Instrumentation and theory, *Appl. Optics*, *23*, 3716–3724.
Shupe, M. D., S. Y. Matrosov, and T. Uttal (2006), Arctic mixed-phase cloud properties derived from surface-based sensors at SHEBA, *J. Atmos. Sci.*, *63*, 697–711.
Shupe, M. D., J. S. Daniel, G. De Boer, E. W. Eloranta, P. Kollias, C. N. Long, E. P. Luke, D. D. Turner, and J. Verlinde (2008), A focus on mixed-phase clouds: The status of ground-based observational methods, *Bull. Am. Meteorol. Soc.*, *89*, 1549–1562.
Smith, W. L., H. M. Woolf, and H. E. Fleming (1972), Retrieval of atmospheric temperature profiles from satellite measurements for dynamical forecasting, *J. Appl. Meteorol.*, *11*, 113–122.
Stephens, G. K., et al. (2002), The CLOUDSAT mission and the A-Train—A new dimension of space-based observations of clouds and precipitation, *Bull. Am. Meteorol. Soc.*, *83*, 1771–1790.
Strabala, K. I., S. A. Ackerman, and W. P. Menzel (1994), Cloud properties inferred from 8-12 μm data, *J. Appl. Meteorol.*, *33*, 212–229.
Sun, Z., and K. P. Shine (1994), Studies of the radiative properties of ice and mixed-phase clouds, *Q. J. R. Meteorol. Soc.*, *120*, 111–137.
Susskind, J., C. D. Barnet, and J. M. Blaisdell (2003), Retrieval of atmospheric and surface parameters from AIRS/AMSU/HSB data in the presence of clouds, *IEEE Trans. Geosci. Remote Sens.*, *41*, 390–409.
Trenberth, K. E., and J. T. Fasullo (2010), Simulation of present-day and twenty-first-century energy budgets of the Southern Oceans, *J. Clim.*, *23*, 440–454.
Verlinde, J., et al. (2007), The mixed-phase Arctic cloud experiment, *Bull. Am. Meteorol. Soc.*, *88*(2), 205–221.
Wang, Z., K. Sassen, D. Whiteman, and B. Demoz (2004), Studying altocumulus plus virga with ground-based active and passive remote sensors, *J. Appl. Meteorol.*, *43*, 449–460.
Wegener, A. (1911), *Thermodynamik der Atmosphäre*, 311 pp., J. A. Barth, Verlag.
Weisz, E., J. Li, J. Li, D. K. Zhou, H.-L. Huang, M. D. Goldberg, and P. Yang (2007), Cloudy sounding and cloud-top height retrieval from AIRS alone single field-of-view radiance measurements, *Geophys. Res. Lett.*, *34*, L12802, doi:10.1029/2007GL030219.

Weng, F. (2007), Advances in radiative transfer modeling in support of satellite data assimilation, *J. Atmos. Sci.*, *64*, 3799–3807, doi:10.1175/2007JAS2112.1.

Wilks, D. S. (1995), *Statistical Methods in the Atmospheric Sciences: An Introduction*, 427 pp., Academic Press, San Diego, Calif.

Winker, D. M., M. A. Vaughan, A. H. Omar, Y. Hu, K. A. Powell, Z. Liu, W. H. Hunt, and S. A. Young (2009), Overview of the CALIPSO mission and CALIOP data processing algorithms, *J. Atmos. Oceanic Technol.*, *26*, 2310–2323, doi:10.1175/2009JTECHA1281.1.

Wiscombe, W. J. (1977), The delta-M method: Rapid yet accurate radiative flux calculations for strongly asymmetric phase functions, *J. Atmos. Sci.*, *34*, 1408–1422.

Wood, R., and J. P. Taylor (2001), Liquid water path variability in unbroken marine stratocumulus cloud, *Q. J. R. Meteorol. Soc.*, *127*, 2635–2662.

Yang, P., K. N. Liou, K. Wyser, and D. Mitchell (2000), Parameterization of the scattering and absorption properties of individual ice crystals, *J. Geophys. Res.*, *105*(D4), 4699–4718, doi:10.1029/1999JD900755.

Zhang, D., Z. Wang, and D. Liu (2010), A global view of midlevel liquid-layer topped stratiform cloud distribution and phase partition from CALIPSO and CloudSat measurements, *J. Geophys. Res.*, *115*, D00H13, doi:10.1029/2009JD012143.

Zhang, Z. (2013), On the sensitivity of cloud effective radius retrieval based on spectral method to bi-modal droplet size distribution: A semi-analytical model, *J. Quant. Spectrosc. Radiat. Transfer*, *129*, 79–88.